

YAWING EFFECTS IN WIND POWER PLANTS: STOCHASTIC WAKE MODELING
AND CONTROL

by

Mireille Rodrigues

APPROVED BY SUPERVISORY COMMITTEE:

Armin Zare, Chair

Mario A. Rotea

Stefano Leonardi

Yaqing Jin

Copyright © 2023

Mireille Rodrigues

All rights reserved

YAWING EFFECTS IN WIND POWER PLANTS: STOCHASTIC WAKE MODELING
AND CONTROL

by

MIREILLE RODRIGUES, BE, ME

THESIS

Presented to the Faculty of
The University of Texas at Dallas
in Partial Fulfillment
of the Requirements
for the Degree of

MASTER OF SCIENCE IN
MECHANICAL ENGINEERING

THE UNIVERSITY OF TEXAS AT DALLAS

August 2023

ACKNOWLEDGMENTS

I would like to thank the many people involved in bringing this research work to completion.

Firstly, I thank my advisor, Dr. Armin Zare for introducing me to the world of flow control in wind energy. I highly appreciate his mentoring, many patient explanations and the time spent in guiding me in my area of research. In addition, I have learnt much from his attention to detail and dedication to good quality and flow of technical writing. I am grateful for the opportunities extended to me by him over the past year as well as the exposure to several new and different aspects of wind power. I also thank Drs. Mario A. Rotea, Stefano Leonardi, and Yaqing Jin for their support as my committee members. Gratitude is extended to Dr. Leonardi and Dr. Federico Bernardoni for the use of LES data to train our models. I thank all my instructors for inspiring me with their passion for their courses. Thanks to the Office of Graduate Education for their help in reviewing this thesis.

I would like to thank my awesome team-mates, especially Aditya Bhatt for his guidance into the existing work, Michael who will be continuing it, and Arya and Amin for their support. A special thanks to the super colleagues and lab-mates that enriched my experience here at UTD and provided some much needed breaks from work, Daniel, Wenqing, Jingbo, Ipsita, David, Nicolas, etc.

I would like to very specially thank my sister, Dr. M. Rodrigues for the huge love, support, guidance, constant pushing and many sacrifices without which much of my progress throughout the course of this degree would not have been possible. A huge thank you is also extended to Shawn and his family for support and encouragement and making me feel welcomed. Thanks to my father, Mr. M.S. Rodrigues for support during my studies. I also credit my late uncle, Sebastiao and my aunts, Liberata and Benedicta for always encouraging me through low points over many years and pushing me to aspire higher.

August 2023

YAWING EFFECTS IN WIND POWER PLANTS: STOCHASTIC WAKE MODELING AND CONTROL

Mireille Rodrigues, MS
The University of Texas at Dallas, 2023

Supervising Professor: Armin Zare, Chair

The success of model-based closed-loop yaw control strategies relies on the accuracy of models that are used to estimate the spatio-temporal attributes of wakes behind wind turbines. We utilize a stochastic dynamical modeling framework to develop reduced-order models of wind farm turbulence that capture the effects of yaw misalignment due to control or atmospheric variability on turbine wakes and their interactions. In this approach, stochastically forced linear models of the turbulent velocity field are used to augment analytical descriptions of the wake velocity provided by low-fidelity engineering wake models. The power-spectral densities of the stochastic models are identified via convex optimization to ensure statistical consistency with high-fidelity large-eddy simulations while preserving model parsimony. We first demonstrate the utility of our approach in capturing turbulence intensity variations at the hub-height of turbines that are yawed against the inflow velocity field impinging on the wind farm. We then extend our two-dimensional (2D) models of hub-height velocity to three-dimensional (3D) wind field models that account for the dynamics of the normal velocity and can thus capture complex attributes of yawed wind turbine wakes such as their rotation and curl. Our results in training 2D and 3D stochastic linear models provide insight into the significance of sparse field measurements in reproducing the statistical signature of wind farm turbulence and demonstrate the robustness of our modeling approach to atmospheric

uncertainties and yaw misalignment effects. In the final part of this thesis, we use actuator disc concepts to demonstrate the utility of infinite-horizon stopping in optimizing the yaw angles of wind turbines for constrained maximum power production.

CONTENTS

ACKNOWLEDGMENTS	iv
ABSTRACT	v
LIST OF FIGURES	ix
CHAPTER 1 INTRODUCTION	1
1.1 Background and motivation	1
1.2 Research objectives	4
1.3 Organization of the thesis	5
CHAPTER 2 ANALYTICAL MODELS FOR WIND TURBINE WAKES	7
2.1 Gaussian deficit model	8
2.1.1 Wake velocity deficit	8
2.1.2 Wake deflection	9
2.1.3 Superposition of waked velocities	10
2.2 Curled wake model	12
2.2.1 Cross-plane velocity components	13
2.2.2 Turbulence Modeling	14
2.2.3 Marching scheme for streamwise perturbation velocity	15
2.3 Curled-skewed wake model	15
2.4 Cumulative curl model	16
CHAPTER 3 STOCHASTIC DYNAMICAL MODELING OF WIND FARM FLOWS	17
3.1 Stochastically forced linearized Navier Stokes equations	17
3.2 Volume penalization	19
3.3 System equations	21
3.4 Boundary conditions	22
3.5 Second-order statistics of model	22
3.6 Formulation of covariance completion problem	25
CHAPTER 4 APPLICATION OF MODELING TECHNIQUE TO TURBULENT FLOWS AROUND YAWED WIND TURBINES	28
4.1 2D deflection model	28

4.1.1	Numerical experiments	29
4.2	3D curl model	31
4.2.1	Numerical experiments	32
CHAPTER 5	INFINITE-HORIZON STOPPING FOR OPTIMAL POWER PRODUCTION IN WIND FARMS	35
5.1	Problem Formulation	35
5.1.1	Actuator disc model	35
5.1.2	Optimization problem	36
5.1.3	Limitations and Assumptions	37
5.2	Wind farm model	38
5.3	Numerical Experiments	38
5.3.1	Wind Farm	38
5.3.2	Infinite horizon stopping cases	39
5.3.3	Monte Carlo simulations	40
5.4	Results	40
CHAPTER 6	CONCLUDING REMARKS	45
6.1	Conclusions	45
6.2	Ongoing efforts	46
APPENDIX A	SUPERPOSITION TECHNIQUES ON IDENTITY FORCED RESULTS	47
APPENDIX B	RESULTS FROM HIGHER MISALIGNMENTS	49
APPENDIX C	COMPARISON STUDY OF CURLED WAKE PARAMETERS	51
C.1	Shear profile at the inflow	51
C.2	Reynolds number	51
C.3	Wake rotation in cross-plane velocity components	52
C.4	Effect of grid size	52
BIBLIOGRAPHY	55
BIOGRAPHICAL SKETCH	61
CURRICULUM VITAE		

LIST OF FIGURES

1.1	Annual and Cumulative growth in U.S. Wind Power Capacity. (source: U.S. Department of Energy [17])	2
1.2	(a) Typical Wind Turbine Generator Design [3] (b) Wind Turbine Plant [62]) .	2
1.3	We propose a dynamical modeling framework that combines the low cost of low-fidelity models with the predictive capability of high-fidelity models.	6
2.1	(a) A schematic of the wake deflection indicating the potential core and path relative to the free stream velocity U_∞ and (b) Streamwise velocity predicted by Equation (2.1) at a misalignment of 30°	9
2.2	The velocity profiles at the hub height of a cascade of 4 turbines under superposition principles Equation (2.3), 2.4 and 2.5 for sub-figures (a), (b) and (c) respectively.	11
2.3	(a) The effect of the cumulative shed vortices on the rotor plane with the rotor projection as the solid black circle. The dashed box shows the region close to the ground elaborated in the figures on the right. (b) Vorticity with ground effects. (c) Vorticity without ground effects.	14
3.1	Process flow diagram for the proposed dynamical modeling framework.	18
3.2	Contour plots of $K^{-1}(x, z)$ used in the volume penalization technique for yaw angles (a) $\gamma = 0$; and (b) $\gamma = 45^\circ$	20
3.3	One point velocity correlations uu and vv on the diagonal and two-point velocity correlations uv on the off-diagonal of the covariance matrix X	24
3.4	A comparison of the streamwise velocity variances uu of a row of 4 turbines yawed at $\gamma = 30^\circ$ from (a) LES and (b) the linearized dynamics (3.4) subject to white-in-time stochastic forcing.	24
3.5	Spatial data training points represented as blue dots in the velocity field.	27
4.1	(a) Layout of wind farm with 4 turbines in a cascade spaced $4d_0$ apart (b) Coefficients of thrust and power versus the tip speed ratio; C_P in blue, C_T in red and the TSR corresponding to the maximum C_P in black	29
4.2	The Streamwise uu (left) and spanwise ww (right) velocity variances at the hub height of a cascade of 4 turbines with uniform yaw angles of 15° (a,b,c,d) and 30° (e,f,g,h) resulting from LES (a,b,e,f) and our stochastic dynamical model (c,d,g,h).	30
4.3	One point velocity correlations uu , vv and ww on the diagonal and two-point velocity correlations uv , vw and uw on the off-diagonal of the covariance matrix X	32
4.4	Top View: The velocity variances at the hub height of a turbine with uniform yaw angles of 15° resulting from LES (a,c,e) and our stochastic dynamical model (b,d,f); uu (a,b), vv (c,d), ww (e,f).	33

4.5	Top View: The velocity covariances at the hub height of a turbine with uniform yaw angles of 15° resulting from LES (a,c,e) and our stochastic dynamical model (b,d,f); uv (a,b), vw (c,d), uw (e,f)..	33
4.6	Side View: The velocity variances at the hub height of a turbine with uniform yaw angles of 15° resulting from LES (a,c,e) and our stochastic dynamical model (b,d,f); uu (a,b), vv (c,d), ww (e,f).	34
4.7	Side View: The off-diagonal velocity covariances at the hub height of a turbine with uniform yaw angles of 15° resulting from LES (a,c,e) and our stochastic dynamical model (b,d,f); uv (a,b), vw (c,d), uw (e,f).	34
5.1	Case I: Total power over iterations of the stopping problem algorithm.	41
5.2	Case I: Initial (red) versus maximum (blue) power outputs for each turbine.	42
5.3	Case II: Total power (represented by the blue line and measured along the y axis on the left hand side) and maximum thrust forces (represented by the red line and measured along the y axis on the right hand side) over infinite horizon iterations. The limiting thrust force is represented as the red dashed line.	42
5.4	Monte Carlo simulations for Case I considering (a) wind variations alone; and (b) wind variations and yaw variations.	43
5.5	Monte Carlo simulations for Case II considering (a) wind variations alone; and (b) wind variations and yaw variations.	44
A.1	The streamwise uu (left) and spanwise ww (right) velocity variances as a result of white-in-time forcing of the linearized dynamics of the hub-height velocity fluctuations for a cascade of 4 turbines. The base velocity profiles are obtained using superposition principles from: first row: Equation (2.3); second row: Equation (2.4); and third row: Equation (2.5).	48
B.1	The streamwise uu (left) and spanwise ww (right) velocity variances at the hub height of a cascade of 4 turbines with uniform yaw angles of 45° (e,f,g,h) resulting from LES (a,b) and our stochastic dynamical model (c,d).	50
C.1	The streamwise velocity profile at $6 d_0$ downstream of the turbine when considering (a) uniform inflow to the turbine, and (b) atmospheric boundary layer inflow.	52
C.2	The streamwise velocity profile at $5 d_0$ downstream of the turbine when considering the atmospheric boundary layer (a, b) and uniform inflow to the turbine (c, d) while using only the shed vortices in the vorticity formulation (a, c) and both shed vortices and the wake rotation vortex in vorticity formulation (b, d).	53
C.3	The streamwise velocity profile at $5 d_0$ downstream of the turbine when considering (a) coarser grid in the streamwise direction, and (b) coarser grid in the spanwise and wall-normal direction.	54

CHAPTER 1

INTRODUCTION

1.1 Background and motivation

Sustainable development goals were adopted by the United Nations in 2015 as a means of encouraging global environmental protection and community well-being by 2030. Within these goals, universal access to affordable and clean energy is listed as one of the means of boosting large-scale healthcare and education facilities, creating jobs, and improving livelihoods [58, 59]. Key to this clean energy movement are renewable energy sources such as solar photovoltaics and wind which respectively accounted for 36% and 41% of the newly added U.S. electricity generation capacity in 2021 [57]. These resources are preferred over less sustainable traditional ones that pollute the environment and are not carbon neutral [16].

Several reports have highlighted the steadily increasing competitiveness of the renewables in the global energy market [28, 19]. Over the past two decades, the cost of electricity generated by renewables has decreased considerably [59, 29] with the cost of wind energy dropping by approximately 20% a year in northern Europe alone. Together with the projected increase in global power demand [18], this decrease in the levelized cost of energy (LCOE)¹ builds a compelling case for expansions in the wind energy sector. These factors have resulted in a steady increase in the wind energy capacity of the U.S over the past 7 years (see Figure 1.1).

A wind turbine produces power by converting the kinetic motion of the wind into the rotational motion of its blades (See Figure 1.2(a)). This leads to a downstream wake region behind the turbine's rotor that is characterized by a drop in the wind velocity and an increased level of turbulence [13], which negatively affect the performance of downstream turbines operating within this region. Specifically, the energy production of downstream

¹The LCOE is a parameter which weighs the lifetime costs of a renewable system against its energy production

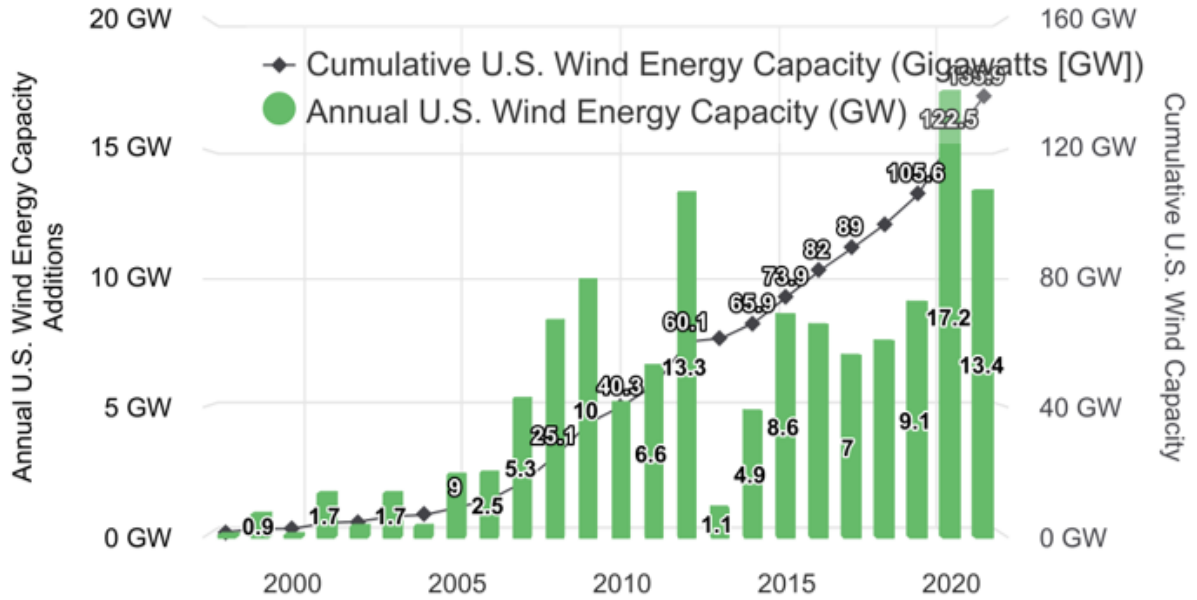


Figure 1.1. Annual and Cumulative growth in U.S. Wind Power Capacity. (source: U.S. Department of Energy [17])

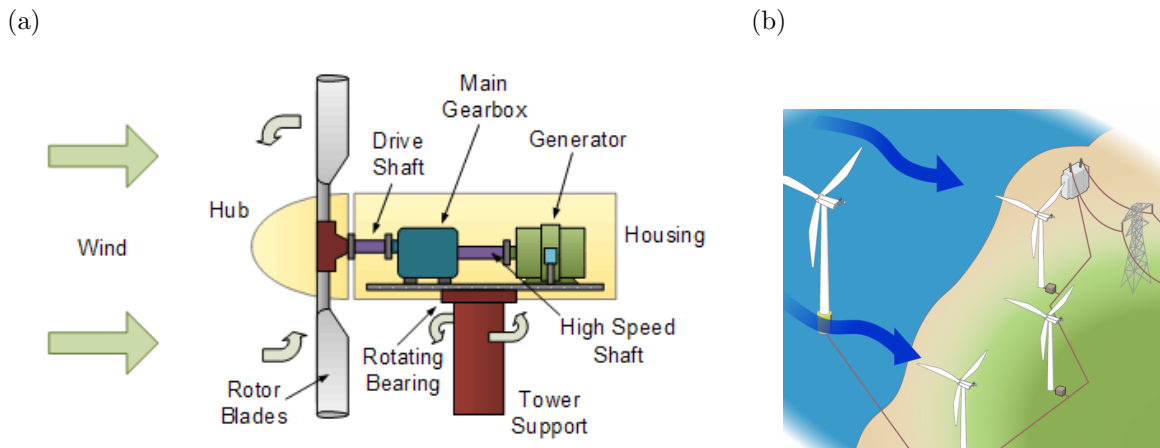


Figure 1.2. (a) Typical Wind Turbine Generator Design [3] (b) Wind Turbine Plant [62])

turbines, which is dependent on their respective incident velocities, is inhibited while structural loading on their towers and blades is increased [13]. It is thus important to mitigate such effects by introducing control capabilities that adjust turbine blade pitch, generator torque, and nacelle direction (yaw). Currently, wind farm operations, which including making adjustments to turbine settings, are aimed at tackling the high variability of atmospheric turbulence using ad-hoc and empirical approaches that may cause plant operations to fall behind optimal conditions. This shortcoming presents an opportunity for the systematic adjustment of turbine setting, e.g., rotor yaw or blade pitch angles, using modern control strategies. An important factor in the success of such endeavours are mathematical models that represent our perception of the incident velocity field for each turbine.

Wind forecasting models can be largely categorized into short-term and long-term models. The while the latter is intended for guiding electricity markets, the former aims to provide predict the direction and speed of incoming wind that is anticipated to impinge upon wind farm turbines. There exist a wide range of forecasting technologies that vary based on their target quantities (e.g., power or wind direction) and the length of their prediction windows. They span from persistence models to numerical weather models to statistical and artificial neural networks-based models [38] to those that adopt hybrid strategies in combining methods [63]. Traditionally, numerical weather models have been used to enable longer-term forecasting, however statistical models are often cheaper and more easily adaptable to smaller wind farms [46]. Thus, in support of short-term wind forecasting strategies that require higher flexibility, there exists a need to combine physics-based concepts, including structural dynamics and fluid mechanics, with statistical modeling techniques, to not only capture quantities of interest that are important in estimation and control of wind farm flows, but to ensure a desirable level of robustness to typically high levels of variability in atmospheric flows.

The study of the fluid mechanics of wind farm flows has relied heavily on medium- and high-fidelity models of wake turbulence such as the Reynolds-averaged Navier-Stokes (RANS)

equations and those used in Large-Eddy Simulations (LES) to low-fidelity models such as the Jensen-Park and Frandsen models. Each class of models presents its own set of conflicting pros and cons when comparing their relative computational cost, fidelity in representing air turbulence, and amenability to control strategies. Simplified engineering wake models of low fidelity incorporate mass and momentum conservation principles to achieve low order representations for the expansion of wakes behind wind turbines and their interactions over wind farms [30, 33, 2]. There have also been efforts to incorporate more complex physical phenomena, e.g., wake rotation, curl, ground effects, and wake mixing, into low-fidelity models [42, 43, 72]. Nevertheless, in the absence of a dynamical model for the fluctuating velocity field, the over-simplified static nature of conventional engineering wake models that neglects the time-varying features of near-field turbulence² leads to the under-prediction of wake recovery [48]. This, in turn, can yield inaccurate predictions of quantities of interest for wind forecasting and turbine control (e.g., the load and power corresponding to each turbine).

1.2 Research objectives

Even though the turbine is at its best efficiency when directly facing the wind inflow, the study of yawed conditions is of critical importance as the rotor is often slow to adapt to directional changes in the incoming wind. Moreover, yaw control strategies have proven vital in improving power capture and reducing structural loads on turbine blades and towers by steering the wake of upwind turbines away from the downwind ones. It is thus important to account for the effects of yawing turbine rotors in the control-oriented modeling of wind farm flows. The effects of the yaw include reducing the wake velocity deficit because of a reduction

²The turbulent flow immediately behind turbine rotors wherein the velocity field is strongly inhomogeneous, sheared, and dominated by the presence of flow structures that are created due to rotor fluid mechanics, e.g., tip vortices [36].

in the total thrust force [6] along with an increase in the deflection angle. In capturing such affects, it is important to aim for two desirable features of an effective control-oriented model: low dimensional and dynamic complexity and robustness. In this thesis, we extend the application of class of stochastic dynamical models that are based on the linearized Navier-Stokes (NS) equations [12, 11] to account for the 3D physical attributes of wind turbine wakes. By linearizing the governing equations, we reduce the dynamic complexity of our models of the wind farm flow. However, this comes at the cost of misrepresenting the complex physics of wake turbulence, which are driven by the nonlinear terms in the NS equations. To overcome this challenge, we introduce an additional degree of freedom through an additive source of stochasticity into the linearized dynamics that we tune via convex optimization to capture critical second-order statistics of the turbulent flow, i.e., normal and shear stresses [66, 64, 68, 65]. On the other hand, due to the physics-based nature of our models they demonstrate a desirable level of robustness to atmospheric changes that may cause a misalignment of the wind direction with the centerline of turbine rotors. The ultimate goal is to provide a class of models that bridge the gap between low-fidelity analytical engineering wake models and high-fidelity models that are based on the nonlinear governing PDEs, e.g., LES; see Figure 1.3. In our work, the results LES are used for both modeling the source of stochasticity that drives our linear dynamics and post-modeling validation. Finally, we take a step toward leveraging the benefits of wake steering on optimal power generation by devising a simple control strategy for yawing wind turbine rotors while respecting structural load limits.

1.3 Organization of the thesis

The thesis is organized as follows. In Chapter 2, we review well-established analytical wake models that have been proposed for capturing the evolution of wakes behind yawed turbines.

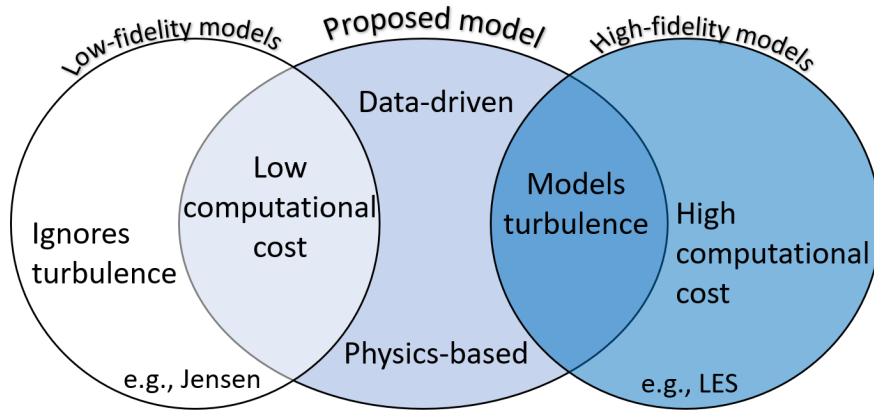


Figure 1.3. We propose a dynamical modeling framework that combines the low cost of low-fidelity models with the predictive capability of high-fidelity models.

In Chapter 3, we summarize a stochastic dynamic framework for the entrainment of second-order statistical signatures of turbulent flows into linear dynamical models that approximate the flow physics. In Chapter 4, we use the modeling framework reviewed in Chapter 3 to develop 2D and 3D stochastic dynamical models of wind farm turbulence that account for the effects of yaw misalignment over various turbines. In Chapter 5, we propose a control strategy for adjusting the yaw angle of individual wind turbines across a given wind farm that is conducive to maximum power production regulated by structural loading limits. Finally, in Chapter 6, we provide a concluding thoughts and highlight potential future directions.

CHAPTER 2

ANALYTICAL MODELS FOR WIND TURBINE WAKES

The structural loading, control aspects and power performance metrics from downstream turbines in a wind farm are heavily dependant on the wake profile that the upstream turbines subject them to. While numerical and experimental techniques are highly accurate in modeling the intricate wake dynamics, analytical models are associated with low computational costs and ease of use. Furthermore, they have matured in formulation over several decades to account for several wake attributes, e.g., wake growth and decay, turbulent mixing, interaction with the ground, and yaw-induced deflection. This makes them ideal for early-stage siting and power production forecasts. As we demonstrate in the following chapters, they can also be used to construct dynamical physics-based models by prescribing base flow profiles for the linearization of the NS equations.

Low-fidelity models of the wake profile are of immense importance in operation of large wind farms as they help predict the power generation losses that partner the misaligned turbine at a lower computational cost. Efforts to accurately model the turbine wakes have seen vast progress in capturing the physics behind wake growth, development and decay downstream to the turbine. In order to maintain the accuracy and robustness of our physics-based model, it is desirable to use the most appropriate representation of the base velocity to adequately linearize the NS equations around.

Incipient research into wake models began with the Jensen model [30] which represented the wake deficit as a top-hat. Subsequently, Katić et al. [33] used this to provide an estimate of the energy contained in the wind field while assuming a constant wake velocity. Following this, was the Frandsen model [21] which used momentum conservation and the wake expansion to account for the downstream velocity deficit. However, the self-similar Gaussian profile observed in wind-tunnel experiments [14, 41, 44] and wind farm data [22, 71] provoked the development of a new analytical model by Bastankhah and Porté-Agel [5, 6]. They extended

this model to yawed turbines that included the spanwise deflection of the wake caused by the lateral force created by the inflow on the yawed rotor disc [6]. Further study into the fluid dynamics of a yawed wake led to the development of the curled wake [7, 42], characterized by curled or kidney-shaped cross-section, formed due to the action of counter-rotating vortex pairs [26]. A number of these models are described in further detail in the following sections. We note that in all cases below, we define each spatial domain to be streamwise in x , spanwise in z , and wall-normal in y .

2.1 Gaussian deficit model

The analytical wake model proposed by Bastankhah and Porté-Agel [5] modeled the velocity deficit in a Gaussian axisymmetric shape, included mass and momentum conservation principles and was verified against LES data and wind-tunnel measurements [15]. An extension of this model [6] was built to account for the effects of the yaw angle γ on the potential core length x_0 and wake deflection δ relative to the free stream velocity U_∞ . The advantages of this model include its consideration of the wake growth k , wake deflection δ and physical constants based on turbulence intensity from experimental data [70].

2.1.1 Wake velocity deficit

The streamwise velocity profile defined across the finite difference domain is given by

$$U(x, y, z) = U_\infty - U_\infty \left(1 - \sqrt{1 - \frac{C_T \cos \gamma}{8 (\sigma_y \sigma_z / d_0^2)}} \right) \times \exp \left(-0.5 \left[\left(\frac{y - y_h}{\sigma_y} \right)^2 + \left(\frac{z - \delta}{\sigma_z} \right)^2 \right] \right) \quad (2.1)$$

where C_T is the thrust coefficient obtained from operating conditions associated with maximum power generation, d_0 is the non-dimensional rotor diameter, y_h is the hub height, and parameters σ_y , σ_z , and δ are used to characterize the geometric aspects of the deflected wake; see Section 2.1.2 for additional details.

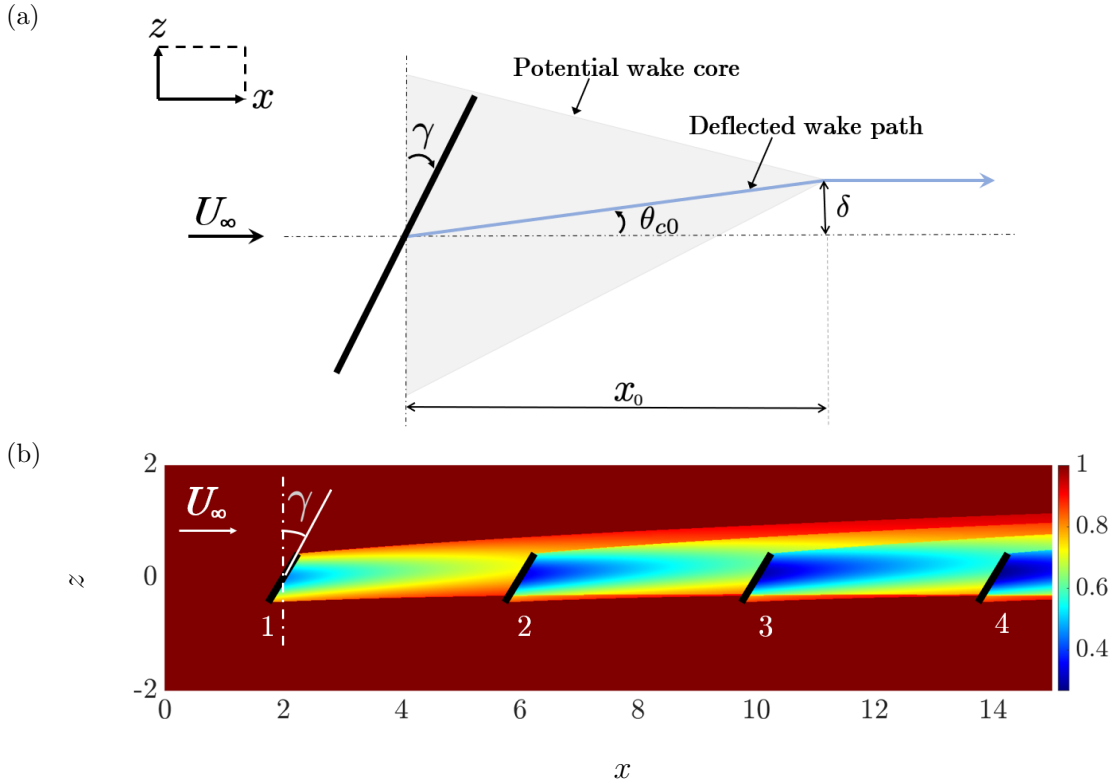


Figure 2.1. (a) A schematic of the wake deflection indicating the potential core and path relative to the free stream velocity U_∞ and (b) Streamwise velocity predicted by Equation (2.1) at a misalignment of 30° .

2.1.2 Wake deflection

The work of Bastankhah and Porté-Agel [6] uses the principle of conservation of momentum to justify the wake deflection away from the center-line of the rotor by arguing that the yawed turbine creates a lateral force on the inflow giving rise to a spanwise velocity that deflects the wake to one side. The potential core is a wake region with uniform velocity and has been conceptualized from the study of coflowing jets. A visual of the wake deflection is illustrated in Figure 2.1(a), where the deflection angle θ_{c0} is given by

$$\theta_{c0} = \frac{0.3\gamma}{\cos\gamma} \left(1 - \sqrt{1 - C_T \cos\gamma}\right)$$

Immediately downstream to the turbine, the potential core becomes smaller in size. This model demarcates the near- and far-wake regions using a potential core length x_0 beyond

which the velocity distribution is self-similar, the core interacts with the ambient flow, and the wake center exhibits recovery.

$$\frac{x_0}{d_0} = \frac{\cos \gamma (1 + \sqrt{1 - C_T})}{\sqrt{2} (4 \alpha I + \beta^* (1 - \sqrt{1 - C_T}))} \quad (2.2)$$

where α and β^* are constants that depend on the turbulence intensity I . The demarcation x_0 is also used to define the deflection δ against the center-line where in the near-wake region ($x \leq x_0$) $\delta := \theta_{c0}(x/d_0)$ and, in the far-wake region ($x > x_0$),

$$\frac{\delta}{d_0} = \theta_{c0} \frac{x_0}{d_0} + \frac{\theta_{c0}}{14.7} \sqrt{\frac{\cos \gamma}{k C_T}} (2.9 + 1.3 \sqrt{1 - C_T} - C_T) \times \ln \left[\frac{(1.6 + \sqrt{C_T}) \left(1.6 \sqrt{\frac{8 \sigma_y \sigma_z}{d_0^2 \cos \gamma}} - \sqrt{C_T} \right)}{(1.6 - \sqrt{C_T}) \left(1.6 \sqrt{\frac{8 \sigma_y \sigma_z}{d_0^2 \cos \gamma}} + \sqrt{C_T} \right)} \right]$$

and the wake widths in the vertical and spanwise directions denoted by σ_y and σ_z , respectively, are given by

$$\begin{aligned} \frac{\sigma_y}{d_0} &= k \frac{x - x_0}{d_0} + \frac{1}{\sqrt{8}} \\ \frac{\sigma_z}{d_0} &= k \frac{x - x_0}{d_0} + \frac{\cos \gamma}{\sqrt{8}}. \end{aligned}$$

2.1.3 Superposition of waked velocities

While the velocity signature of a single turbine can be defined by its deficit in a relatively straightforward manner, the cumulative effect of overlapping wakes results in regions that experience enhanced levels of deficit. Such interactions between wind turbine wakes are typically accounted for using superposition techniques on the deficits of the interacting wakes [48].

Three common superposition techniques are described as

$$U_i = U_\infty - \sum_k (U_\infty - U_{ki}), \quad (2.3)$$

$$U_i = U_\infty - \sqrt{\sum_k (U_\infty - U_{ki})^2}, \quad (2.4)$$

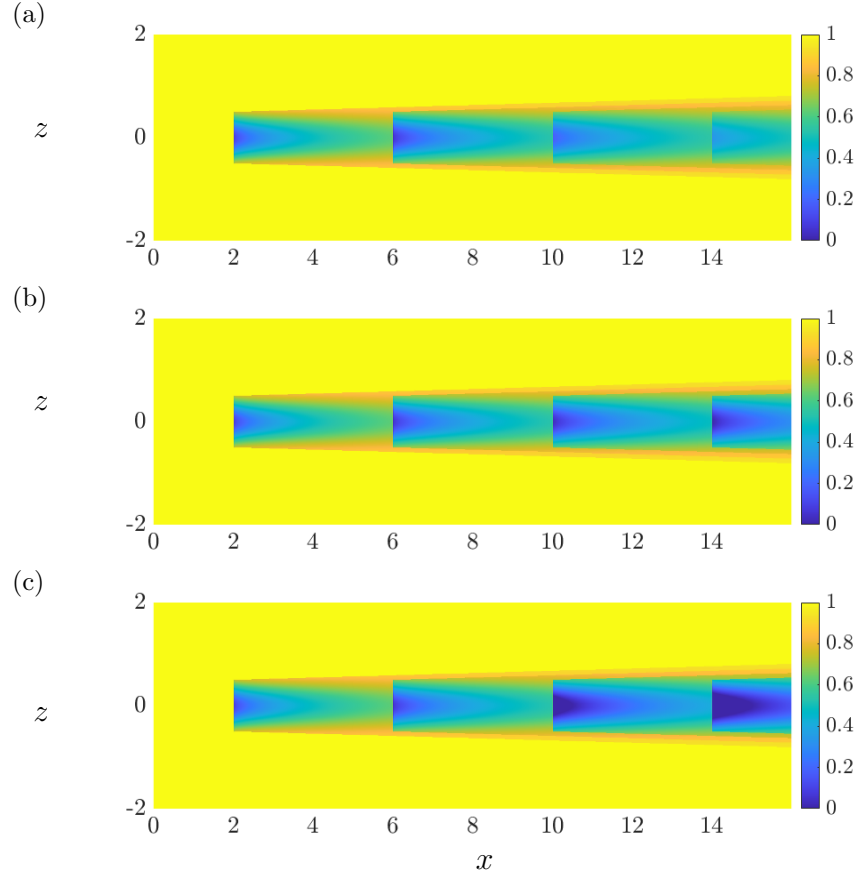


Figure 2.2. The velocity profiles at the hub height of a cascade of 4 turbines under superposition principles Equation (2.3), 2.4 and 2.5 for sub-figures (a), (b) and (c) respectively.

$$U_i = U_\infty - \sqrt{\sum_k (U_k - U_{ki})^2}. \quad (2.5)$$

where U_i is the velocity incident to each turbine in the array, U_∞ is the free stream velocity and U_{ki} is the wake velocity of turbine k at the location of turbine i . Equation (2.3) models the velocity deficit based on linear superposition of the velocity deficits [39] while Equations 2.4 [33] and 2.5 [60] assume that the kinetic energy deficit is summed over the relevant upstream turbines considering the difference of the wake velocity against the free-stream and inflow to each turbine, respectively. Figure. 2.2 shows the result of applying these superpo-

sition techniques for capturing the waked velocity deficits due to wake interactions within a cascade of turbines.

2.2 Curled wake model

The Gaussian deficit model is ill-equipped to represent the fluid dynamics and physics that affect the wakes. This is because for yawed turbines and yawed porous discs in uniform flow, counter-rotating vortex pairs (CVP) were observed as the wake traveled downstream [26] leading to a spanwise asymmetry in the wake shape. To address this issue, Bastankhah et al. [7] developed the wake edge as an ideally thin vortex sheet that moved in time with the flow. In this model, the vortex sheet was calculated as power series expansion and marched downstream in the direction of the free-stream velocity. Their model also considered the physics resulting from ground effects and wake deflection. In this section, we provide details on an alternative curled wake profile that is adapted from the model given by Martínez-Tossas et al. [42].

The curled wake model that we adopt considers a velocity field that is split into a static component $[U \ V \ W]^T$ and perturbations induced by the rotation of the yawed turbine $[u' \ 0 \ 0]^T$. The streamwise component of the static velocity U denotes the atmospheric boundary layer profile and the wall-normal V and spanwise W components capture the cumulative effect of a number of counter-rotating vortices that are shed from the yawed turbine. We note that the perturbation to the wall-normal and spanwise velocities are of little consequence to the wake deformation (i.e., $v' = w' = 0$). Assuming the pressure gradient to be zero, the NS equation can be simplified to the following

$$U \frac{\partial u'}{\partial x} + V \frac{\partial (U + u')}{\partial y} + W \frac{\partial u'}{\partial z} = \nu_{eff} \left(\frac{\partial^2 u'}{\partial x^2} + \frac{\partial^2 u'}{\partial y^2} + \frac{\partial^2 u'}{\partial z^2} \right) \quad (2.6)$$

where ν_{eff} is the effective viscosity. In what follows, we describe the equations for cross-plane terms (V and W) in addition to details on the effective viscosity ν_{eff} and the numerical

scheme we use to march Equation (2.6). We investigate certain changes to the curled wake parameters described in the sections below on the base velocity field of this model in Appendix C.

2.2.1 Cross-plane velocity components

The distinctive kidney-shape of the curled wake profile results from wall-normal V and spanwise W velocity components that are due to the interaction of a number of counter-rotating vortices that are shed from a yawed rotor disc and a wake rotation vortex that captures the rotational movement within the disc area. The cumulative effect of the counter-rotating vortices are reflected in analytical expressions for the streamwise and spanwise velocities, i.e.,

$$V = \sum_{i=1}^N \frac{y_i \Gamma_i}{2\pi (y_i^2 + z_i^2)} \left(1 - e^{-(y_i^2 + z_i^2)/\sigma^2}\right) \quad (2.7)$$

$$W = \sum_{i=1}^N \frac{z_i \Gamma_i}{2\pi (y_i^2 + z_i^2)} \left(1 - e^{-(y_i^2 + z_i^2)/\sigma^2}\right) \quad (2.8)$$

where N is the number of individual shed vortices, Γ_i is the strength of each vortex, and σ is the size of the vortex core. The total circulation strength Γ is given by

$$\Gamma = \frac{\pi}{8} \rho D U_\infty C_T \sin(\gamma) \cos^2(\gamma). \quad (2.9)$$

To preserve the total circulation and to ensure that each vortex has an individual strength relative to its distance from the rotor center, we use the following relations for the strength of each vortex.

$$\Gamma_i = -4\Gamma_0 \frac{r_i^2}{ND^2 \sqrt{1 - (2r_i/D)^2}} \quad (2.10)$$

where $\Gamma_0 = 4/\pi\Gamma$. Another contributor to the cross-plane velocity components is the wake rotation which consists of a tangential velocity distribution within the rotor disc area, which

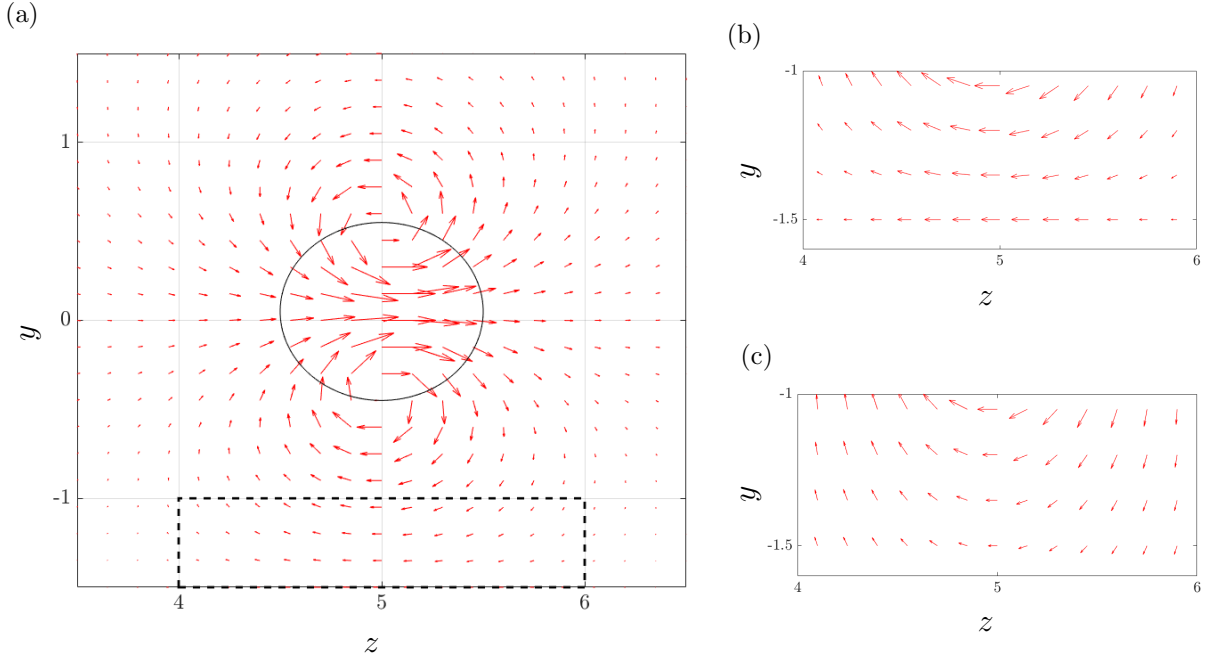


Figure 2.3. (a) The effect of the cumulative shed vortices on the rotor plane with the rotor projection as the solid black circle. The dashed box shows the region close to the ground elaborated in the figures on the right. (b) Vorticity with ground effects. (c) Vorticity without ground effects.

is computationally modeled as a single vortex of circulation strength

$$\Gamma_{wr} = 2\pi (a - a^2) U_\infty D / \lambda \quad (2.11)$$

where a is the induction factor based on the thrust coefficient and λ is the tip speed ratio. Ground effects can also be incorporated into the model by mirroring the shed vortices with respect to the ground. Figure 2.3 depicts how the quiver plots for the cross-plane velocities change close to the ground if ground effects are captured.

2.2.2 Turbulence Modeling

We assume the effective viscosity ν_{eff} from Equation 2.6 to be the sum of a turbulent viscosity $\nu_T = l_m^2 |du/dz|$ with $l_m = \kappa z \frac{1}{(1 + \kappa z / \lambda)}$ representing the mixing length [50] and a

stabilizing viscosity ν_{Re} based on the Reynolds number, which can be computed as

$$\nu_{Re} = \frac{UD}{Re}. \quad (2.12)$$

2.2.3 Marching scheme for streamwise perturbation velocity

The velocity field is subject to a streamwise perturbation velocity u' at the rotor plane that represents the initial deficit as the wind hits the rotor. Within the rotor, this profile is set to $-2aU_\infty$ and is smoothed (e.g., using a Gaussian filter) to zero at the boundaries. From this initial condition, we march the streamwise perturbation downstream by discretizing Equation (2.13) using a first-order upwind scheme in the streamwise direction and second-order finite differencing scheme in the cross-plane directions. This yields the discretized variant of the equations as

$$u'_{[i+1,j,k]} = u'_{[i,j,k]} - \frac{\Delta x}{(U + u')_{[i,j,k]}} \left(V_{[i,j,k]} \frac{(U + u')_{[i,j+1,k]} - (U + u')_{[i,j-1,k]}}{\Delta y} + \right. \quad (2.13)$$

$$\left. W_{[i,j,k]} \frac{u'_{[i,j,k+1]} - u'_{[i,j,k-1]}}{\Delta z} - \nu_{eff} \nabla^2 u'_{[i,j,k]} \right)$$

2.3 Curled-skewed wake model

The models detailed in Sections 2.1 and 2.2 assume a purely streamwise inflow, however the actual wind inflow to a turbine is rarely comprised of a single velocity component. This calls for a modeling framework that incorporates the vertical change in wind direction (or veer) into the waked velocity profile of a turbine. Seminal attempts into modeling the veer into the wake profiles [1] were built upon skewing the Gaussian wake model, deflecting the wake as a function of the height-related inflow velocity. The veer model proposed by Mohammadi et al. [47], can be obtained by two means, the first applies the deflection technique to the vortex-sheet curled wake model [7]; and the second, which factors the veer into the wind direction and yaw misalignment. As such complicated wake models do not contribute the

outcome of this thesis, we refrain from providing further details on such models and refer the interested reader to the original references.

2.4 Cumulative curl model

The extension of the aforementioned curled wake models to wind farms is erroneous as they do not account for the yaw-added wake recovery and the secondary steering effects of the counter-rotating vortices. Recent efforts in analytical modeling techniques depict a sophisticated representation of wake interactions and involve the study of the long-range decay and atmospheric interactions of the curled wakes. The Gauss-curl hybrid model [35] and the Cumulative-curl wind-farm model [8] are noteworthy in this respect, in terms of their predictions of the wake velocity and power predictions in larger wind farms [35]. As such complicated wake models do not contribute the outcome of this thesis, we refrain from providing further details on such models and refer the interested reader to the original references.

CHAPTER 3

STOCHASTIC DYNAMICAL MODELING OF WIND FARM FLOWS

In this chapter, we provide details of a stochastic dynamical modeling framework that uses analytical wake models and is informed by high-fidelity simulations to model wind farm turbulence. We describe the linearized NS equations and the implementation of a volume penalization technique for accounting for the presence of turbine structures within the velocity field. We then identify the power-spectral density of stochastic forcing into the linearized dynamics by solving a convex optimization problem that ensures that certain velocity correlations are matched in accordance with high-fidelity LES. This proposed modeling framework follows the flowchart detailed in Figure 3.1.

3.1 Stochastically forced linearized Navier Stokes equations

The engineering wake models in Chapter 2 provide analytical expressions for the velocity field that capture various structural aspects of spatially expanding wakes that are formed behind wind turbines. These predictions of static models may constitute a basic velocity profile around which fluctuations of the velocity field evolve. Based on this, the total wind velocity field \mathbf{u} can be decomposed into the sum of the static base flow $\bar{\mathbf{u}}$ predicted by an above engineering wake model and velocity fluctuations \mathbf{v} that evolve around $\bar{\mathbf{u}}$, i.e.,

$$\mathbf{u} = \bar{\mathbf{u}} + \mathbf{v}, \quad \bar{\mathbf{u}} = \mathbf{E}[\mathbf{u}], \quad \mathbf{E}[\mathbf{v}] = 0 \quad (3.1)$$

where $\mathbf{E}[\cdot]$ is the time-averaged operator.

The dynamics of small velocity and pressure fluctuations (\mathbf{v}, p) around a base flow determined by $(\bar{\mathbf{u}}, \bar{P})$ are governed by the linearized NS and continuity equations

$$\mathbf{v}_t = -(\nabla \cdot \mathbf{v}) \bar{\mathbf{u}} - (\nabla \cdot \bar{\mathbf{u}}) \mathbf{v} - \nabla p + \frac{1}{Re} \Delta \mathbf{v} - K^{-1} \mathbf{v} + \mathbf{d} \quad (3.2)$$

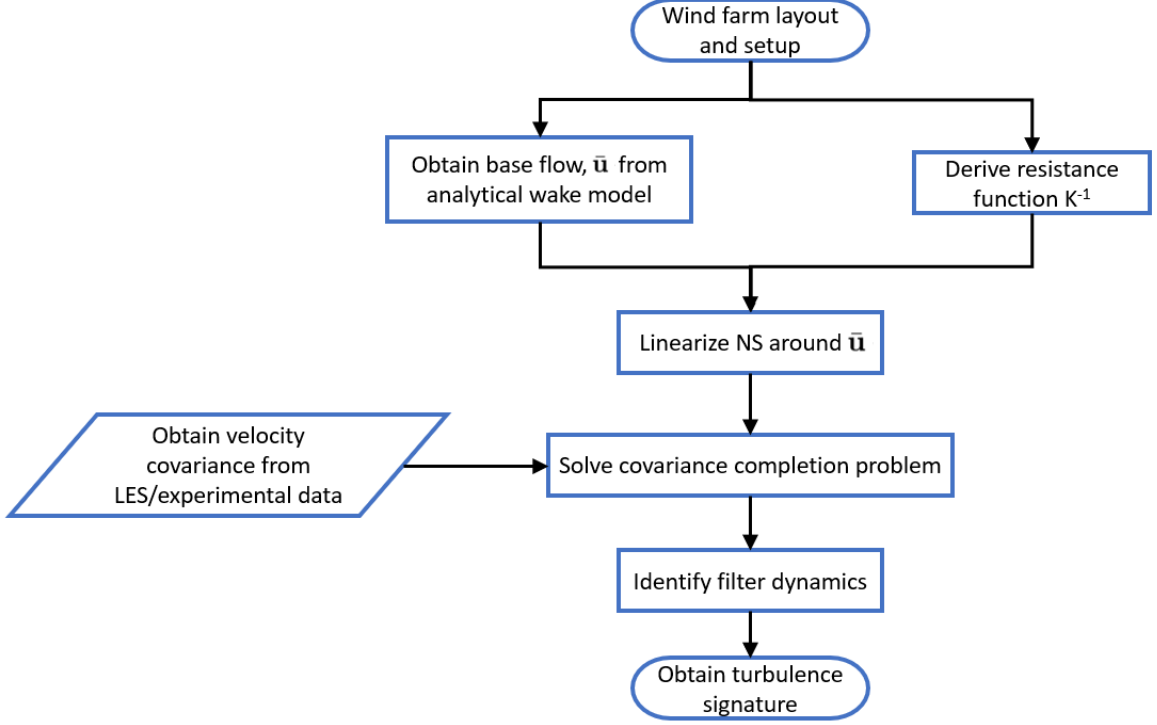


Figure 3.1. Process flow diagram for the proposed dynamical modeling framework.

$$0 = \nabla \cdot \mathbf{v} \quad (3.3)$$

where the base flow has a single non-zero component in the streamwise direction resulting from an engineering wake model (e.g., Equation (2.1)), i.e., $\bar{\mathbf{u}} = [\bar{U} \ \bar{V} \ \bar{W}]^T$, $\mathbf{v} = [u \ v \ w]^T$ is the fluctuating velocity vector, with components u , v and w denoting the velocity in the streamwise (x), wall-normal (y) and spanwise (z) directions, respectively, and \mathbf{d} is a zero-mean stationary stochastic input that is used to trigger a statistical response from the linearized dynamics. Here, ∇ is the gradient operator, $\Delta = \nabla \cdot \nabla$ is the Laplacian, and the Reynolds number is defined in terms of the rotor diameter d_0 , the free-stream velocity U_∞ , and the kinematic viscosity ν as $Re = U_\infty d_0 / \nu$ (from Equation (2.12)). In the NS equations (Equations 3.2, 3.3), length, velocity, time, and pressure have been non-dimensionalized by d_0 , U_∞ , d_0/U_∞ , and ρU_∞^2 , respectively.

To bring Equation (3.2) to a state-space form, we follow a standard conversion for the elimination of pressure together with finite-dimensional approximation of the differential operators [32, 65]. This is done by first eliminating pressure by applying the divergence operator to Equation (3.2), which is then simplified by using the continuity equation (Equation (3.3)) resulting in a partial differential equation for the evolution of \mathbf{v} . The evolution of the vorticity can be obtained by finding the curl of Equation (3.2). Applying a Fourier transform allows us to rewrite the equations in state-space form where the turbulence \mathbf{v} is the state of the system and the A , B and C operators are defined in Section 3.3. We obtain $\bar{\mathbf{u}}$ from an appropriate analytical wake model and the system equation now provides us with the evolution of the turbulence as follows

$$\dot{\mathbf{v}}(t) = A\mathbf{v}(t) + B\mathbf{d}(t). \quad (3.4)$$

The form of system matrices A and B , along with details of the employed finite-dimensional approximation and boundary conditions on \mathbf{v} can be found in [11, Appendix A]. The stochastic input \mathbf{d} provides a degree of freedom for shaping the statistics of the velocity field \mathbf{v} . In what follows, we provide details on structural constraints that govern the statistics of the state \mathbf{v} and input \mathbf{d} in system (3.4).

3.2 Volume penalization

Equations (3.2) use a volume penalization technique to model the effect of solid obstructions to the flow caused by turbine structures. Instead of resolving the grid and implementing no-slip/no-penetration boundary conditions over the surface of turbine structures, this method allows us to capture the effect of turbine rotors and nacelles (and even turbine towers in 3D models) by penalizing the velocity field using the negative feedback term $K^{-1}\mathbf{v}$. In this approach K plays the role of a permeability function that only affects the velocity field

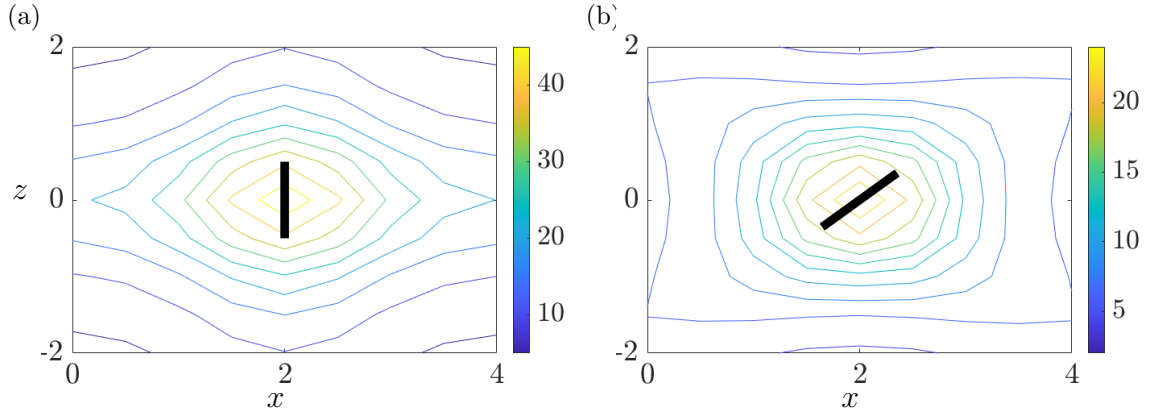


Figure 3.2. Contour plots of $K^{-1}(x, z)$ used in the volume penalization technique for yaw angles (a) $\gamma = 0$; and (b) $\gamma = 45^\circ$.

at or around the coordinates of solid structures and has no influence on the flow at other spatial locations; see [34] for details.

Within the fluid $K \rightarrow \infty$ so that the penalization resulting from $K^{-1}\mathbf{v}$ does not influence the flow. This would yield back the original linearized NS dynamics. On the other hand, within solid structures $K \rightarrow 0$ so that the negative feedback forces the velocity field to zero. To capture the spatial region that is influenced by the presence of the turbines, we use a smooth 2D filter function of the form $K^{-1}(x, z) = f(x)h(z)$ with

$$f(x) = \frac{c}{\pi} [\arctan(a(x - x_1)) - \arctan(a(x - x_2))]$$

$$h(z) = \frac{c}{\pi} [\arctan(a(z - z_1)) - \arctan(a(z - z_2))]$$

Here, $x_{1,2}$ and $z_{1,2}$ determine the spatial extent of the rotors in the horizontal plane and parameters a and c determine the slope and magnitude of the function, respectively [52]. To apply this function correctly to a yawed turbine, the grid points are rotated by the yaw angle and new yawed spatial limits (x_1, x_2, z_1, z_2) are defined. A contour plot is shown in Figure 3.2 indicating how this function changes when a turbine reorients itself from zero misalignment to one of 45° .

3.3 System equations

The system matrices in Equation (3.4) are dependant upon the dimensionality of the domain as well as the number of velocity components that are being considered while linearizing the NS equations. As an example, the system matrices are listed below for a 2-D domain in x and z while considering only a streamwise base velocity component $\bar{\mathbf{u}}$, turbulence $\mathbf{v} = [u \quad w]$ and assuming that cross-flow base velocity terms are negligible.

$$\begin{aligned}
\mathbf{A} &= \Delta^{-1} \begin{bmatrix} A_{11} & A_{12} \\ A_{21} & A_{22} \end{bmatrix}, \\
A_{11} &= -\bar{\mathbf{u}} \Delta \partial_x - \bar{\mathbf{u}}_x \Delta - 2\bar{\mathbf{u}}_{xz} \partial_z - \bar{\mathbf{u}}_{zz} \partial_x - \bar{\mathbf{u}}_{xzz} + \frac{1}{Re} \Delta^2, \\
A_{12} &= -\bar{\mathbf{u}}_{zzz} + \bar{\mathbf{u}}_z \Delta + \bar{\mathbf{u}}_{xz} \partial_x - 2\bar{\mathbf{u}}_{zz} \partial_z, \\
A_{21} &= 2\bar{\mathbf{u}}_x \partial_{xz} + \bar{\mathbf{u}}_{xz} \partial_x + \bar{\mathbf{u}}_{xxz} + \bar{\mathbf{u}}_{xx} \partial_z, \\
A_{22} &= -\bar{\mathbf{u}}_{xx} \partial_x - \bar{\mathbf{u}}_x \Delta \partial_x - 2\bar{\mathbf{u}}_x \partial_{xx} + \bar{\mathbf{u}}_{zz} \partial_x - \bar{\mathbf{u}}_{xzz} + \frac{1}{Re} \Delta^2, \\
\mathbf{B} &= \Delta^{-1} \begin{bmatrix} B_{11} & B_{12} \\ B_{21} & B_{22} \end{bmatrix}, \\
B_{11} &= \mathbf{f}_{xx} + 2\mathbf{f}_x \partial_x + \mathbf{f} \partial_{xx}, \\
B_{12} &= -(\mathbf{f}_{xz} + \mathbf{f}_x \partial_z + \mathbf{f}_z \partial_x + \mathbf{f} \partial_{xz}), \\
B_{21} &= -(\mathbf{f}_{xz} + \mathbf{f}_x \partial_z + \mathbf{f}_z \partial_x + \mathbf{f} \partial_{xz}), \\
B_{22} &= \mathbf{f}_{xx} + 2\mathbf{f}_x \partial_x + \mathbf{f} \partial_{xx}
\end{aligned}$$

where, $\mathbf{f}(x, z)$ in matrix B is a 2D shape function that determines the spatial extent of the forcing. The suffixes x and z denote the partial derivatives in space. For discretization of the domain and finite-dimensional approximation of the differential operators in the system matrices above, we use a second-order central differencing scheme with N_x and N_z uniformly distributed collocation points in the streamwise and spanwise directions, respectively.

3.4 Boundary conditions

Besides at the inlet and outlet, we implement homogeneous Dirichlet and Neumann boundary conditions at all other edges of our computational domain. At the inlet and outlet of the domain along the streamwise dimension, we apply linear extrapolation conditions (see [51] for details). For a 2D model of the hub-height velocity field, these boundary conditions take the following form:

$$\begin{aligned}
\mathbf{v}(x, z(1)) &= \mathbf{v}(x, z(N_z)) = 0 \\
\mathbf{v}_x(x, z(1)) &= \mathbf{v}_x(x, z(N_z)) = \mathbf{v}_z(x, z(1)) = \mathbf{v}_z(x, z(N_z)) = 0 \\
\mathbf{v}(x(1), z) &= \alpha \mathbf{v}(x(2), z) + \beta \mathbf{v}(x(3), z), \\
\mathbf{v}(x(N_x), z) &= \alpha \mathbf{v}(x(N_x - 1), z) + \beta \mathbf{v}(x(N_x - 2), z), \\
\mathbf{v}_x(x(1), z) &= \alpha \mathbf{v}_x(x(2), z) + \beta \mathbf{v}_x(x(3), z), \\
\mathbf{v}_x(x(N_x), z) &= \alpha \mathbf{v}_x(x(N_x - 1), z) + \beta \mathbf{v}_x(x(N_x - 2), z), \\
\mathbf{v}_z(x(1), z) &= \alpha \mathbf{v}_z(x(2), z) + \beta \mathbf{v}_z(x(3), z), \\
\mathbf{v}_z(x(N_x), z) &= \alpha \mathbf{v}_z(x(N_x - 1), z) + \beta \mathbf{v}_z(x(N_x - 2), z)
\end{aligned}$$

where

$$\alpha = \frac{x(N_x) - x(N_x - 2)}{x(N_x - 1) - x(N_x - 2)}, \quad \beta = \frac{x(N_x - 1) - x(N_x)}{x(N_x - 1) - x(N_x - 2)}.$$

Note that in the case of an equally spaced grid, $\alpha = 2$ and $\beta = -1$. We also introduce sponge layers at the inflow and outflow to mitigate the influence of boundary conditions on the fluctuation dynamics within the computational domain [49, 40, 53].

3.5 Second-order statistics of model

Under steady atmospheric conditions, the global operator A in Equation (3.4) is stable. Thus, if (A, B) is a controllable pair, the steady-state covariance of the fluctuating velocity

field

$$X = \lim_{t \rightarrow \infty} \mathbf{E} [\mathbf{v}(t) \mathbf{v}^*(t)] \quad (3.5)$$

resulting from persistent stochastic excitation of the linear dynamics solves the Lyapunov-like equation

$$A X + X A^* = -B H^* - H B^*. \quad (3.6)$$

This equation relates the statistics of the state to the spectral content of the stochastic input. The entries of X represent two-point correlations of the velocity field at various spatial locations across the wind farm, with diagonal entries denoting one-point correlations or the intensity of the turbulent flow. In Equations (3.5) and (3.6), $*$ denotes the complex conjugate transpose and matrix H quantifies the cross-correlation between the input and the state [68, Appendix B], i.e.,

$$H := \lim_{t \rightarrow \infty} \mathbf{E} [\mathbf{v}(t) \mathbf{d}^*(t)] + \frac{1}{2} B \Omega.$$

For zero-mean white-in-time forcing \mathbf{d} with covariance Ω , i.e., $\mathbf{E}[\mathbf{d}(t)] = 0$ and $\mathbf{E}[\mathbf{d}(t) \mathbf{d}^*(\tau)] = \Omega \delta(t - \tau)$, $H = (1/2) B \Omega$ and Equation (3.6) reduces to the standard algebraic Lyapunov equation

$$A X + X A^* = -B \Omega B^*.$$

As we demonstrate in Figure 3.4(b), white-in-time stochastic input \mathbf{d} with covariance $\Omega = I$ result in streamwise and spanwise velocity correlations that are quite different from that of an LES-generated velocity field (Figure 3.4(a)). As an exercise, we also consider the effect of the superposition techniques (defined in Section 2.1.3) on the base velocity field of our wind farm model to the sensitivity of the modeling framework subject to white-in-time forcing in Appendix A.

When we assume that the input is zero-mean (i.e. $\mathbf{E}[\mathbf{d}(t)] = 0$) and white-in-time with covariance Ω , (i.e. $\mathbf{E}[\mathbf{d}(t) \mathbf{d}^*(t)] = \Omega$), H reduces to $(1/2) B \Omega$. This brings Equation (3.6) to the standard algebraic Lyapunov equation form.

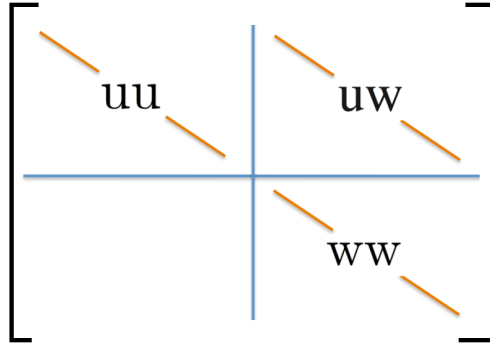


Figure 3.3. One point velocity correlations uu and vv on the diagonal and two-point velocity correlations wv on the off-diagonal of the covariance matrix X .

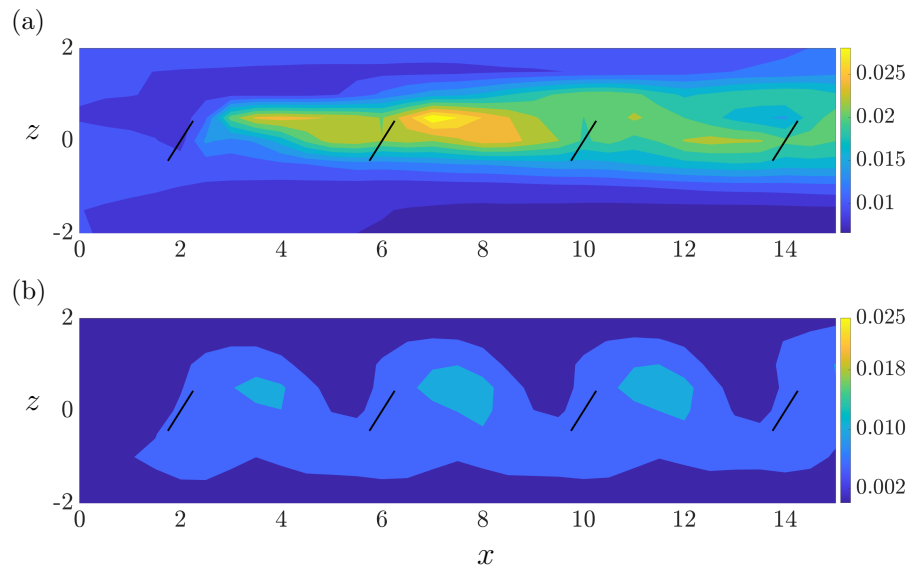


Figure 3.4. A comparison of the streamwise velocity variances uu of a row of 4 turbines yawed at $\gamma = 30^\circ$ from (a) LES and (b) the linearized dynamics (3.4) subject to white-in-time stochastic forcing.

3.6 Formulation of covariance completion problem

Better estimates of the velocity covariance levels can be obtained via a stochastic realization informed by velocity statistics at prespecified wind farm locations. To this end, we adopt the stochastic dynamical modeling framework of Zare et al. [64, 68, 65], which has shown success in estimating the statistical signature of wind farm turbulence when turbine rotors are perpendicular to the wind direction [12, 11].

The velocity statistics that we use to train our stochastic models may be gathered via field experiments using, e.g., LiDAR measurement devices, or may result from high-fidelity LES simulations. As mentioned in the previous subsection, the one-point velocity correlations represent diagonal entries and the two-point velocity correlations represent off-diagonal entries of covariance matrix X . We seek input matrix B and statistics of forcing \mathbf{d} that induce a statistical response from the linearized dynamics (3.4) that reproduces the partially known statistics. This information can be obtained from the solution to the covariance completion problem

$$\begin{aligned} & \min_{X,Z} -\log \det (X) + \alpha \|Z\|_* \\ & \text{subject to } AX + XA^* + Z = 0 \\ & X_{i,j} = G_{i,j}, \quad \forall \{i,j\} \in \mathcal{I} \end{aligned} \tag{3.7}$$

which penalizes a composite objective subject to two linear constraints that (i) ensure statistical consistency with model (3.4) via the Lyapunov-like equation, and (ii) match partially known second-order statistics of the velocity field. In this convex optimization problem, Hermitian matrices X and Z are optimization variables, and entries of G corresponding to the set of indices \mathcal{I} represent partially available second-order statistics of the output \mathbf{v} . The objective function establishes a trade-off (weighted by the parameter $\alpha > 0$) between the solution to a maximum-entropy problem, which uses the logarithmic barrier function to

ensure positive definiteness of matrix X , and a nuclear norm regularizer, which is used as a convex proxy for the rank function (see, e.g., [20, 54]). The rank of matrix Z bounds the number of independent input channels or columns in matrix B thereby providing a means to regulate the complexity of the forcing model as colored-in-time forcing \mathbf{d} that excites all degrees of freedom can completely overwrite the linearized dynamics [64].

The solution to problem (3.7) can be used to realize the appropriate colored-in-time forcing \mathbf{d} of system (3.4) such that the partially available velocity correlations are reproduced. Specifically, the matrix Z resulting from problem (3.7) can be decomposed into matrices B and H (see Equation (3.6)) via spectral decomposition techniques [64, Section III.B]. While matrix H can be used to construct a low-pass filter that generates the suitable colored-in-time forcing \mathbf{d} , matrix B determines how such forcing enters the linear dynamics (3.4). The spatio-temporal realization of colored-in-time forcing \mathbf{d} can be equivalently interpreted as a white-in-time excitation together with a data-enhanced dynamical modification to the linearized dynamics in the form of a state-feedback interaction; see [67, 64] for additional details.

The parameterization of stochastic forcing relies on the solution to problem (3.7) and is thereby affected by the available training data (correlations of streamwise u and spanwise w velocity) indicated by set \mathcal{I} . As a result atmospheric changes that may result in rapid variations in the intensity and direction of wind can jeopardize the validity of estimations provided by a stochastic model that is developed using a set of velocity correlations at prespecified wind farm locations. In the next section, we use a sequence of streamwise and spanwise velocity correlations from immediately behind turbine rotors to develop a stochastic model of wind farm turbulence. We then evaluate the robustness of our 2D and 3D models to yaw misalignments that influence correlation patterns throughout the farm.

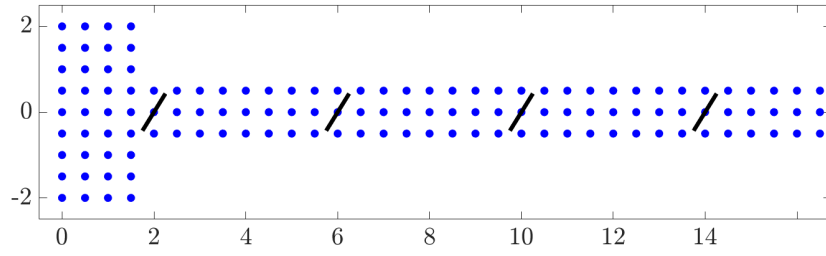


Figure 3.5. Spatial data training points represented as blue dots in the velocity field.

CHAPTER 4

APPLICATION OF MODELING TECHNIQUE TO TURBULENT FLOWS

AROUND YAWED WIND TURBINES

The stochastic dynamic modeling framework established in Chapter 3 is now used to predict the second-order velocity statistics in a wind farm using some of the wake models described in Chapter 2. We first present a 2D model of the hub-height velocity field for a cascade of 4 turbines in Section 4.1. We then extend the model to account for the velocity field around a stand-alone turbine in Section 4.2.

4.1 2D deflection model

We first consider a setup of a cascade of 4 turbines that are uniformly yawed against the wind direction behaving according to the Gaussian deficit model [6] described in Section 2.1.1 pictured in Figure 4.1(a). This model can be reduced to two dimensions and still display the deficit and the spanwise deflection from the wake center, therefore, our computational domain is a hub-height section of the velocity field. Our computational field spans $x \in [0, 15]$ and $z \in [-2, 2]$ and the turbines are placed at $z = 0$ with a spacing of $4d_0$. The first turbine is at $x = 2$. The grid spacing for the finite difference model is set to $0.5d_0$ in spanwise and streamwise directions.

When considering a hub-height cross-sectional domain, Equation (2.1) can be reduced to

$$U(x, z) = U_\infty - U_\infty \left(1 - \sqrt{1 - \frac{C_T \cos \gamma}{8 (\sigma_y \sigma_z / d_0^2)}} \right) e^{-0.5 \left[\frac{z - \delta}{\sigma_z} \right]^2}. \quad (4.1)$$

Here, $d_0 = 1$ denotes the non-dimensionalized rotor diameter and the wake growth rate is taken as $k = 0.022$. Consistent with the high-fidelity LES that generates the statistical dataset used for modeling, we consider a 5MW NREL [31] turbine at maximum power production with a thrust coefficient of $C_T = 0.7871$ (see Figure 4.1(b)), a Reynolds number of

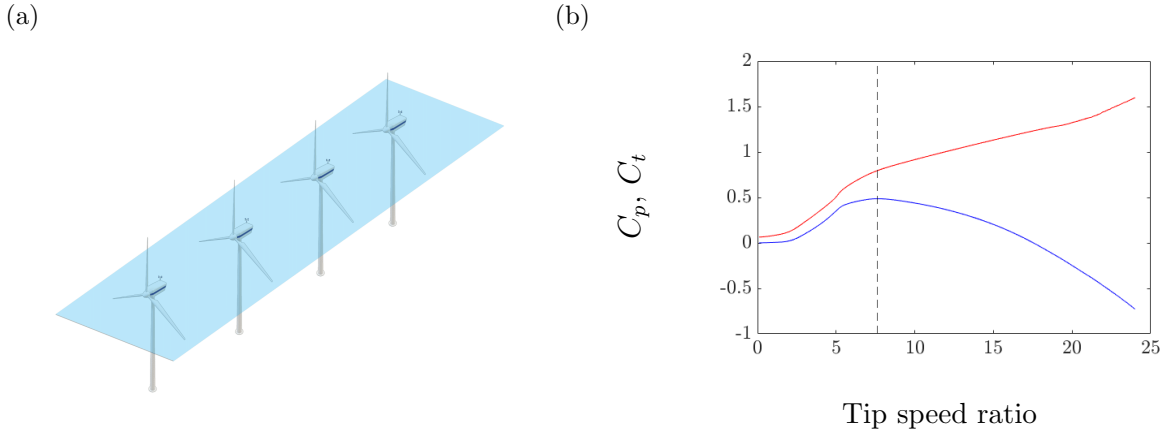


Figure 4.1. (a) Layout of wind farm with 4 turbines in a cascade spaced $4d_0$ apart (b) Coefficients of thrust and power versus the tip speed ratio; C_P in blue, C_T in red and the TSR corresponding to the maximum C_P in black

10^8 , and an incoming turbulence intensity of $I = 0.08$. Following [6], the constant $\beta^* = 0.154$ in Equation (2.1.2) is determined under ideal conditions with no incoming turbulence ($I = 0$) to match the potential core length x_0 of jet flows. The turbulence intensity, $\alpha = 2$ is computed to best approximate the potential core length in accordance with the results of LES of flow behind a single turbine for various yaw angles.

4.1.1 Numerical experiments

Following previous work in modeling velocity variances for a similar setup of a wind farm, we provide access to flow statistics up to 3 diameters downstream to each turbine with 3 training points across its span [11] (see Figure 3.5). The results of the covariance completion is seen in Figure 4.2 for streamwise and spanwise velocity covariances for yawed cases of $\gamma = 15^\circ$ and 30° . The plots indicate that the dominant features, from high to low energies, are being captured by our stochastic model, even though a few spurious regions of high energy are also displayed. The results display the pair of intensity streams from the rotor tips for the 15° case and the single stream for the 30° case. In particular, we observe traits such as the slight asymmetry and surge of the streamwise intensity streams resulting from

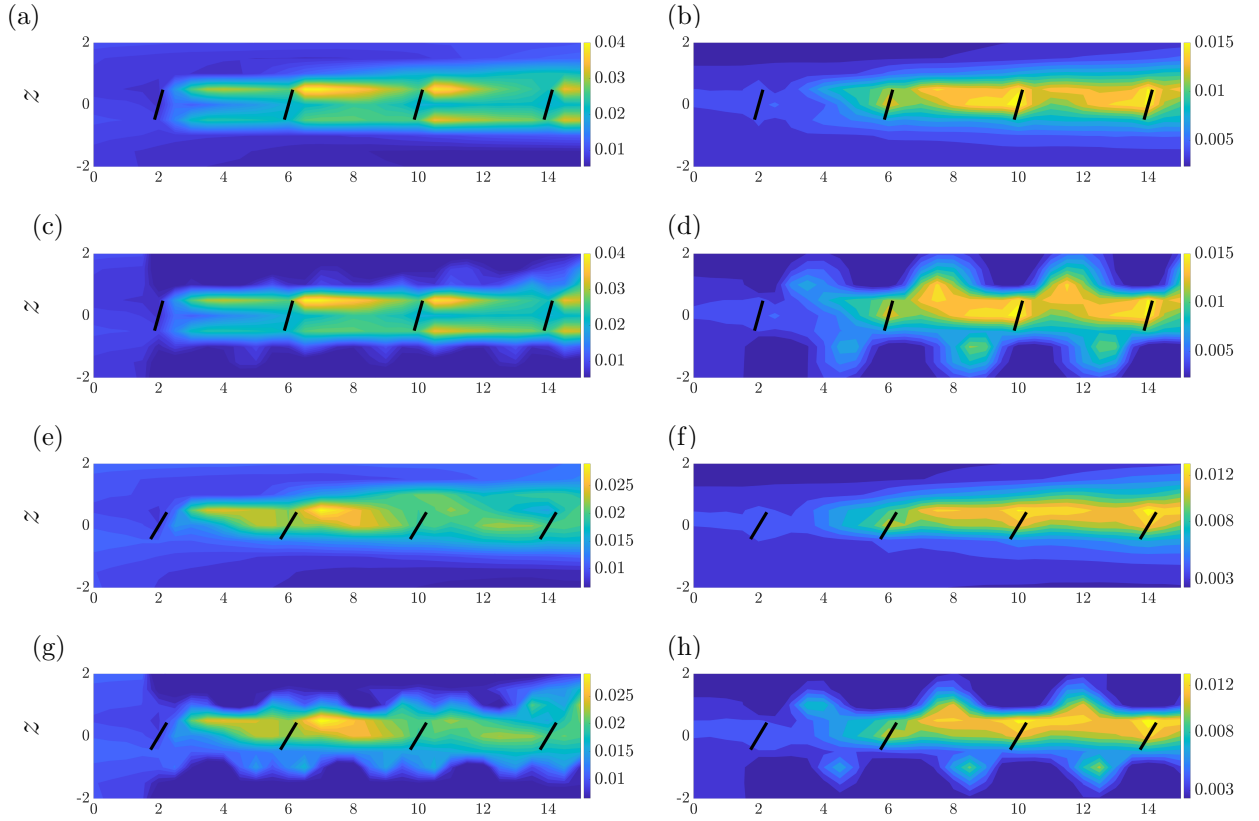


Figure 4.2. The Streamwise uu (left) and spanwise ww (right) velocity variances at the hub height of a cascade of 4 turbines with uniform yaw angles of 15° (a,b,c,d) and 30° (e,f,g,h) resulting from LES (a,b,e,f) and our stochastic dynamical model (c,d,g,h).

the turbines rotation and its eventual dissipation just ahead of the immediate downstream turbine. For the spanwise intensities ww we observe that spurious regions exist beyond the blade tips but the predictions of the model hold within the vicinity of the training points. We investigate the velocity variances for a large yaw misalignment of 45° under the same parameters in Appendix B.

The quality of completion of the results is noteworthy in the fact that the training data is spaced away from the trajectory of the wakes thereby establishing this method as a strong contender in turbulence modeling and forecasting. We attribute the robustness of the model, in this respect, to its inherent physics-based nature which complements the optimization

problem. The quality of completion results is also a testament to suitability of the number of training points and their location with respect to the turbine placement.

4.2 3D curl model

The Gaussian wake profile can be adapted to a 2D computational domain, but cannot capture physical aspects of the flow including wake rotation, ground effects and the shear profile of the velocity inflow. We therefore expand our framework to a 3D domain to implement the curled wake profile [42] described in Section 2.2 as our baseline velocity. For the sake of compactness, we limit the numerical experiments to a yaw misalignment of 15° .

The setup of the velocity field for the 3D curl model involves a single turbine at a yaw of 15° . While the base velocity $\bar{\mathbf{u}}$ calculated by Equation (2.13) requires a broad domain of $3d_0$ in the cross-plane directions to maintain the numerical stability of the model, the stochastic dynamical model used a smaller window centered around the turbine rotor to enhance computation ease and time.

In generating the vorticity profile, we approximate 100 tip vortices are generated within the rotor diameter with a vortex contributing to the wake rotation. The spanwise and wall-normal velocity components are assumed to be non-decaying in the streamwise direction in this experiment. Each vortex has a core of $d_0/5$. Following with our case of maximum power output, we take the fluid density to be 1.225 kg/m^3 [13] and the induction factor a for optimized operation is $1/3$. The Reynolds number considered for the effective viscosity is 10^8 . In modeling the turbulent viscosity we take the von Kármán constant to be 0.4 and the recommended mixing length of 15 m [42]. We also extend the Dirichlet and Neumann boundary conditions described in Section 3.4 along the edges of wall normal dimension.

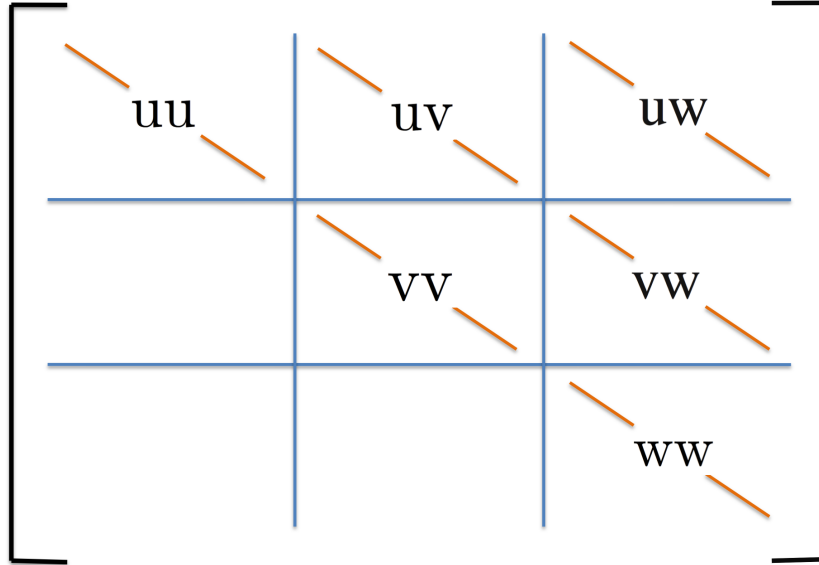


Figure 4.3. One point velocity correlations uu , vv and ww on the diagonal and two-point velocity correlations uv , vw and uw on the off-diagonal of the covariance matrix X

4.2.1 Numerical experiments

For the 3D results, we expand our considerations of velocity correlations to the one point and two point velocity correlations of the covariance matrix X as depicted in Figure 4.3. The results of the covariance completion is seen in Figures 4.4 to 4.7 for the top and side profile views of the domain, each sectioned at the hub.

We note the good quality of completion in the velocity variances uu , vv and ww throughout the domain. The dominant features of the flow are captured such as the asymmetric streams of turbulence from the rotor tips in the top view profiles (see Figure 4.4). We also see the peaks in the velocity variances close to the hub in the side views (see Figure 4.6).

For the velocity covariances uv , vw and uw , we again note a good match in the features of the flow. In particular, we are able to capture the velocity profiles within the vicinity of the training points (see Figures 4.5 and 4.7). The regions outside the training points do show slightly spurious turbulence values in the case of uv , but the overall distinctiveness of the LES simulations are retained.

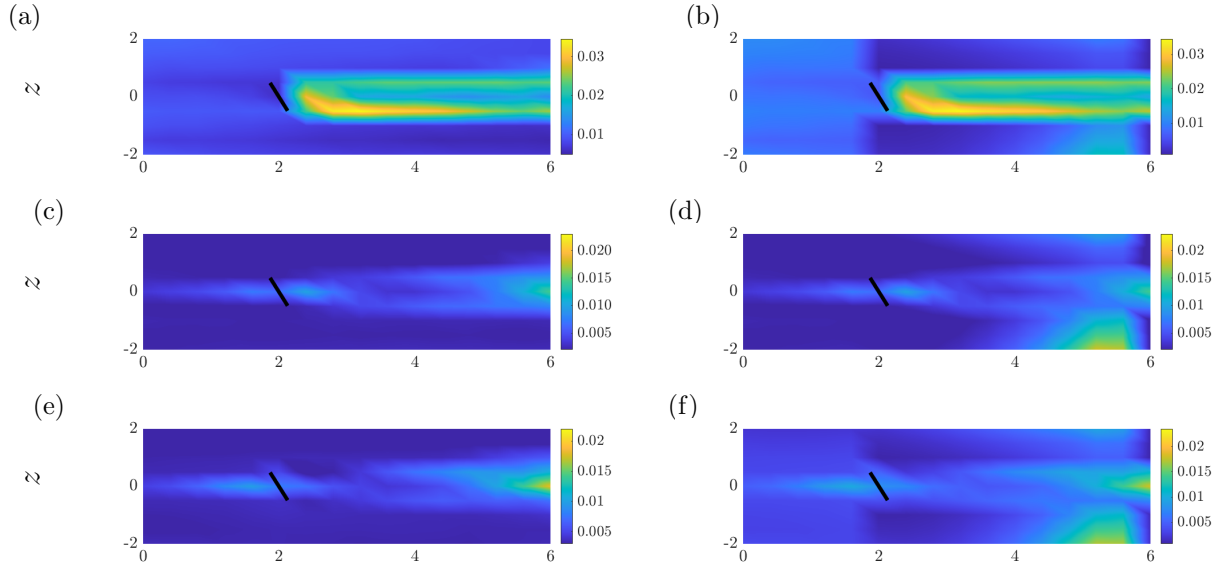


Figure 4.4. Top View: The velocity variances at the hub height of a turbine with uniform yaw angles of 15° resulting from LES (a,c,e) and our stochastic dynamical model (b,d,f); uu (a,b), vv (c,d), ww (e,f).

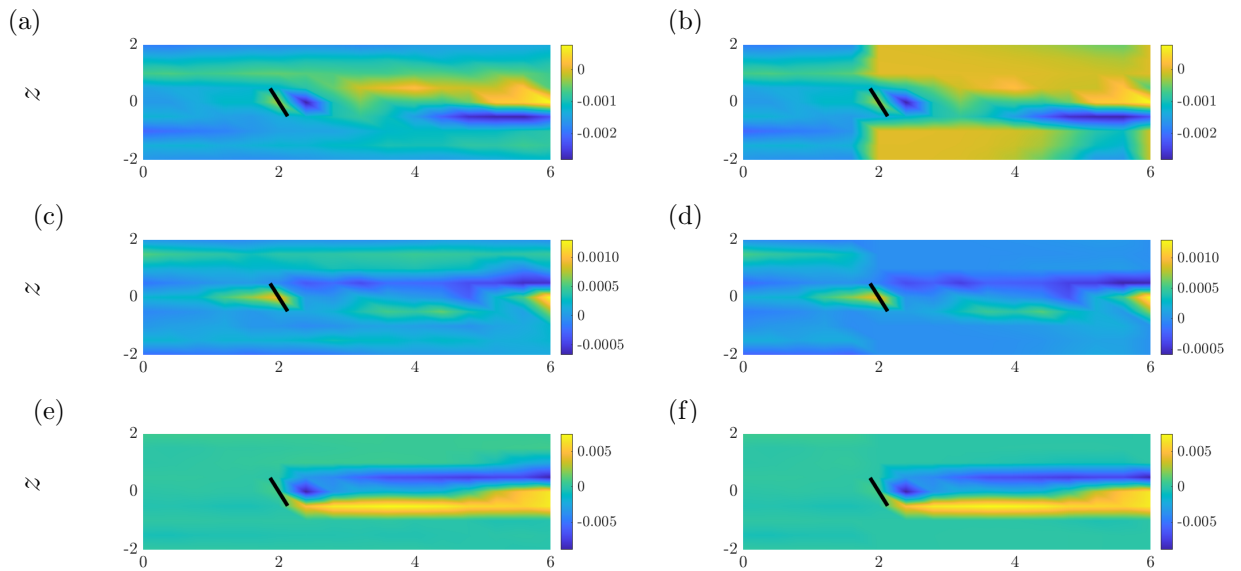


Figure 4.5. Top View: The velocity covariances at the hub height of a turbine with uniform yaw angles of 15° resulting from LES (a,c,e) and our stochastic dynamical model (b,d,f); uv (a,b), vw (c,d), uw (e,f)..

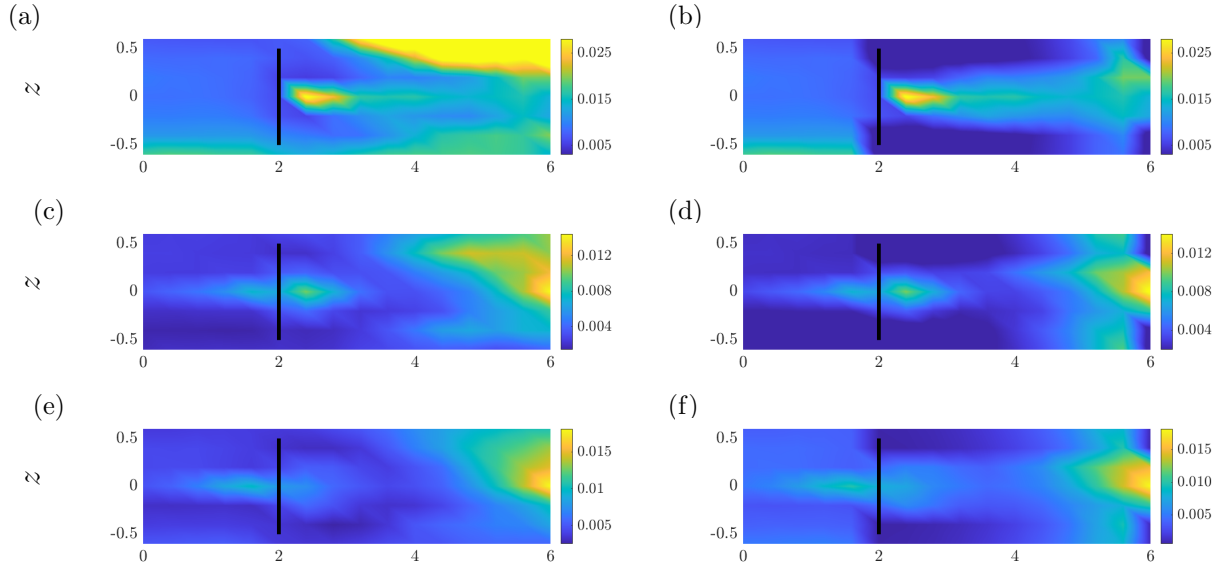


Figure 4.6. Side View: The velocity variances at the hub height of a turbine with uniform yaw angles of 15° resulting from LES (a,c,e) and our stochastic dynamical model (b,d,f); uu (a,b), vv (c,d), ww (e,f).

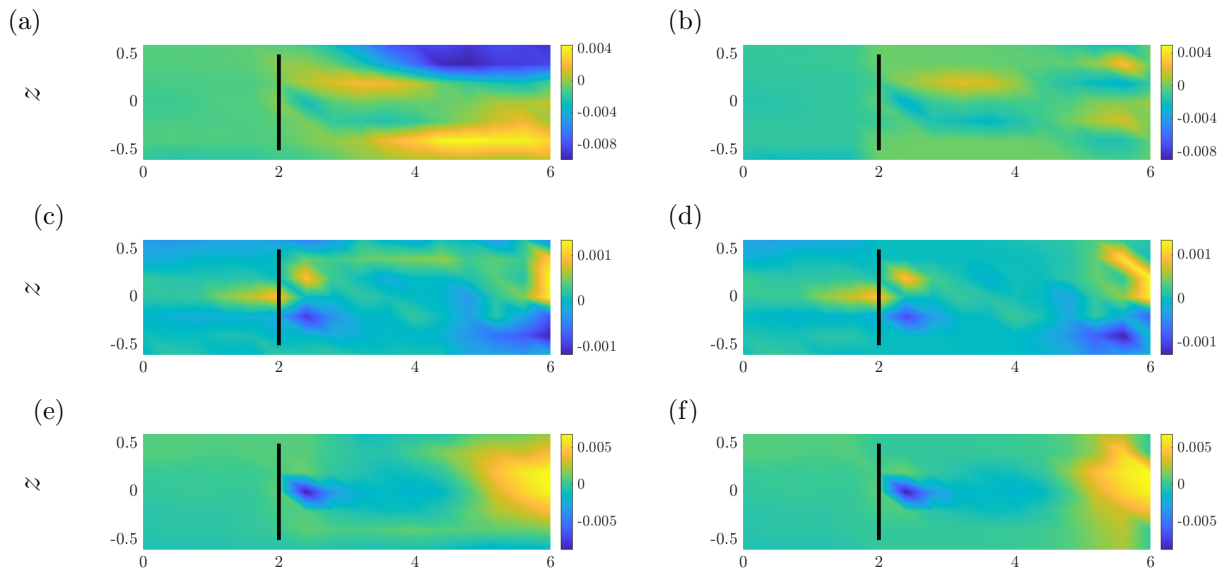


Figure 4.7. Side View: The off-diagonal velocity covariances at the hub height of a turbine with uniform yaw angles of 15° resulting from LES (a,c,e) and our stochastic dynamical model (b,d,f); uv (a,b), vw (c,d), uw (e,f).

CHAPTER 5

INFINITE-HORIZON STOPPING FOR OPTIMAL POWER PRODUCTION IN WIND FARMS

In this chapter, we demonstrate how the yaw of turbine rotors can be adjusted to overcome the negative effects of velocity deficits caused by the operation of upstream wind turbines on the power production and structural loads across wind farms. Based on Equation (2.1), this deficit can be reduced (to a certain extent) by misaligning the rotors against the direction of the wind. However, quantities of interest in the control of wind farms, e.g., thrust force and power, may be negatively impacted by yawing the turbines. The optimal operation of a wind farm entails maximum power production while regulating the strain of component loads across the farm. To address this problem, we formulate an infinite horizon stopping problem [10] to find optimal yaw angles for turbines that are aligned in a cascade. We complement with Monte Carlo simulations that allow us to analyze the robustness of the identified control policy and long-term power estimations to wind speed variations and yawing errors.

5.1 Problem Formulation

We use the Actuator disc model principle to formulate our calculations of quantities of interest. We then define our system and how we apply our optimization problem to it.

5.1.1 Actuator disc model

From the Actuator disc model (ADM) concept, the rotor is represented as a porous disc through which the wind flows [13]. We assume that the entire rotor witnesses a uniform velocity inflow and ignore wind shear. Conservation principles of mass, momentum and energy are applied to the fluid passing through the rotor leading to the calculation of quantities

such as the force exerted on the actuator disc and the power extracted from the wind as shown below:

$$F = \frac{1}{2} \rho A C_T u^2, \quad (5.1)$$

$$P = \frac{1}{2} \rho A C_P u^3. \quad (5.2)$$

Here, F is the thrust force, P is the produced power, ρ is the fluid density, A is the projected area of the disc. C_T and C_P are the coefficients of thrust and power, respectively.

5.1.2 Optimization problem

Following previous state-space representations relevant to optimal control problems [45], we define the system states x to be the incident velocities, \bar{u} to each turbine. The control parameters are taken to be the yaw angle γ for each turbine. Our endeavor to safely maximize the collective power output over a series of turbines leads us to formulate a finite-state infinite horizon problem to decide the yaw angle for each turbine. We seek a combination of yaw control settings that maximizes our value function (given by Equation (5.4)) over an infinite number of stages [10].

Our stage cost g is the total wind farm power output, which is dependant on the state x and control γ and is determined by summing the power across all turbines.

$$g(x, \gamma) = \sum_i P_i. \quad (5.3)$$

Here, P is the power calculated from Equations (5.1) and (5.2) at each turbine i . We define two cases of interest; Case I to exhibit the effect of yaw control on the total power production using Equation (2.1), and Case II to maximize the power production under a limiting thrust force. Therefore, in Case I, we define the value function

$$J(x) := \max_{\gamma} g(x, \gamma) \quad (5.4)$$

and in Case II, we consider the same value function subject to a constraint on the thrust forces, i.e.,

$$J(x) := \max_{\gamma} g(x, \gamma), \quad \text{s.t.} \quad \max_i (F_i) \leq F_{lim} \quad (5.5)$$

where F_i is the thrust force at turbine i which is constrained by an upper limit of F_{lim} .

We consider only yaw angles up to 40° that are conducive to power production in real-world conditions [27], and to avoid Bellman’s curse of dimensionality [9], we discretize our control inputs by limiting them to multiples of 5° . The input and control spaces are therefore, the Euclidean spaces \mathfrak{R}^N and \mathfrak{R}^9 , respectively, where N is the number of turbines. The infinite horizon stopping model here is designed to achieve convergence when improvements to the value function cease to rise beyond a set threshold.

5.1.3 Limitations and Assumptions

- We ignore the vertical shear profile of the wind and any possible horizontal wind veer and consider a single incident velocity into the rotor which is obtained by averaging Equation 2.1 over the hub and rotor tips in a 2D plane;
- We consider only positive yaw angles, in multiples of 5° to aid computations such that $\mathcal{U} = \{0^\circ, 5^\circ, \dots, 40^\circ\}$;
- We penalize the thrust force and power computations from Equations (5.1) and (5.1) on account of the yaw using the projected area of the yawed disc.
- We are neglecting the dynamics of the turbulent flow within the wind farm and assuming the incident velocities upon each turbine to be the output of a static wake deficit model.

5.2 Wind farm model

The incident velocity into each turbine is a key term in the quantities of power and thrust force (Equations (5.1) and (5.1)). It is therefore important to select a model that reasonably depicts the true wake velocity including its physical aspects such as downstream recovery to the free-stream velocity, growth in the spanwise directions, and the aerodynamic coupling from their interactions with other wakes in the velocity field. With considerations to the 2D nature of this model, we note that the low fidelity analytical wake model provided by Bastankhah and Porté-Agel [6], which is applicable to yawed turbine rotors, best suits our purpose. Reference equations for the waked velocity from Section 2.1 serve to provide us with the incident velocities for the downstream turbines for any combination of yaw angles γ_i . We maintain the same non-dimensionality principles as earlier, i.e., the length, velocity and pressure are non-dimensionalized against the rotor diameter d_0 , the free stream velocity U_∞ , and the pressure ρU_∞^2 where ρ is the air density. The thrust coefficient C_T is chosen to correspond to the maximum power coefficient C_P as obtained from large eddy simulations of a 5MW NREL wind turbine; see Section 5.3.1 and Figure 4.1(b) for details.

5.3 Numerical Experiments

5.3.1 Wind Farm

Our quantities of interest, namely power and thrust force, are dependant on incident velocities and projected areas, therefore, we calculate the incident velocities as the velocities experienced at each turbine location assuming a 2D computational domain at the hub-height of turbines. As such, additional discretization points that would provide the velocities between the turbines would only burden the computational time of this problem with no added benefit to accuracy. The wind farm comprises four turbines positioned in a row with a uniform spacing of $4d_0$.

We model the turbine based on operating parameters applicable to the maximum power case for a 5MW NREL turbine [31] modeled using a high fidelity LES code [55, 56] which are applicable to the constant terms in the equations listed in Section 5.2. Since, we consider power production as one of our main concerns, the coefficient of thrust, C_T corresponds to the tip speed ratio that results in the highest possible coefficient of power (also called optimal tip-speed ratio [6]) C_P and is taken to be 0.7871 and 0.5 respectively. The rate of downstream wake growth k is considered to be 0.022 in both, span-wise and wall normal directions, i.e. vertical and horizontal directions when facing the turbine. In calculating the potential core length x_0 , we select α as 2 to match against the turbulence intensity I which is 8% of the free-stream velocity. β^* is taken to be 0.154 based on studies to match the potential core length of jet flows under ideal conditions of no incoming turbulence [6]. We use the Lissaman [39] superposition principle penalizing the velocity deficits as described in Equation 2.3.

5.3.2 Infinite horizon stopping cases

Within this study, we consider two cases of operation and thus develop two infinite horizon stopping models. In Case I, we optimize the power output alone as we seek to demonstrate that maximizing the total power often leads one turbine to sacrifice its performance for the sake of the team. In Case II, we consider a more practical objective of safely maximizing the power under a limiting thrust force (here, considered to be 90% of the maximum thrust force). This constraint is crucial to the safe and efficient operation of turbines as high thrust forces inevitably lead to high component loads [23] that may shorten the required 20 year lifespan of onshore turbines [25]. Following the optimal control problems laid out in Section 5.1.2, we consider different initial conditions (i.e., initial turbine orientations) and record the number of iterations that are required to achieve the optimal policy for Cases I and II.

5.3.3 Monte Carlo simulations

We acknowledge that, most depictions of fluid fields decompose the velocity to the sum of a mean velocity \bar{u} and a velocity fluctuation term v . We obtain \bar{u} from the methodology described in Section 5.2. Accurate turbulence models are generally informed through high-fidelity simulations or through analytical methods [37] while the turbulence velocity is taken to be zero-mean stochastic term with a range informed from our turbulence intensity I . Additionally, in practice, the operation of a wind turbine also includes aspects such as yaw error $\Delta\gamma$, which results in production losses [4, 61]. The uncertainty in these two parameters leads us to the representations of the total velocity and yaw as

$$u = \bar{u} + \Delta u \tag{5.6}$$

and

$$\gamma = \bar{\gamma} + \Delta\gamma \tag{5.7}$$

respectively. After obtaining our ideal yaw angles, we seek to find the sensitivity of our long term power production outlook to the uncertainty provided by wind turbulence and yaw errors. To this end, we consider separate Monte Carlo simulations that account for the uncertainty due to the wind speed alone (Δu) or both wind speed and yaw ($\Delta\gamma$) variations.

5.4 Results

The development of the two cases in this study was intended to firstly, exhibit the effects of the wake interactions on the overall power output of the wind farm, and secondly, to respect component safety in our attempt to optimize wind farm power output. Given that we operate under the assumption of a steady-state velocity field, we seek a convergence of an optimal policy under all initial conditions. While this may be achieved through a computationally less complex permutation problem (i.e., exhaustive search), the solution

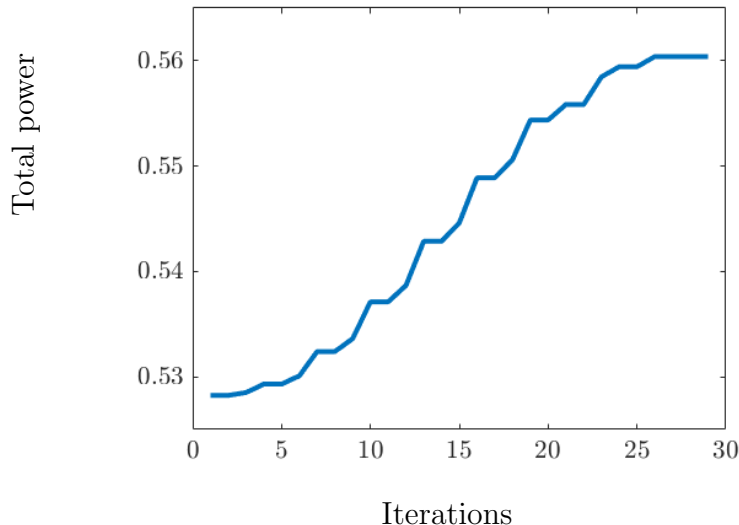


Figure 5.1. Case I: Total power over iterations of the stopping problem algorithm.

to our wind plant setup would entail 9^4 scenarios that cover 9 different yaw angles across 4 turbines even in the absence of parametric variations. For various initial misalignment angles (even those that are very far from the optimal parameters), our approach results in a significant computational benefit whereby solutions are obtained in under 100 iterations. Our results show that in both cases, the last turbine orients itself perpendicular to the free-stream wind direction to capture the maximum possible energy from the wind as it has no turbine behind it to negatively influence and also, that the cumulative wake interactions have significantly lowered the incident wind velocity. We next discuss the outcomes of each case study.

Case I: The optimal policy for the case in which our sole objective is to maximize the power is found to be a misalignment of 40° for the first 2 turbines, 30° for the third and no misalignment for the last turbine. Given uniformly zero initial yaw angles, the power rises by over 20%. Figure 5.1 show the progressive increase in total power as a result of algorithmic updates to the turbine orientations. Figure 5.2 shows how the increase in yaw for the first turbine, which reduces its power production, can increase production over the subsequent turbines. The converged total power calculations from the Monte Carlo

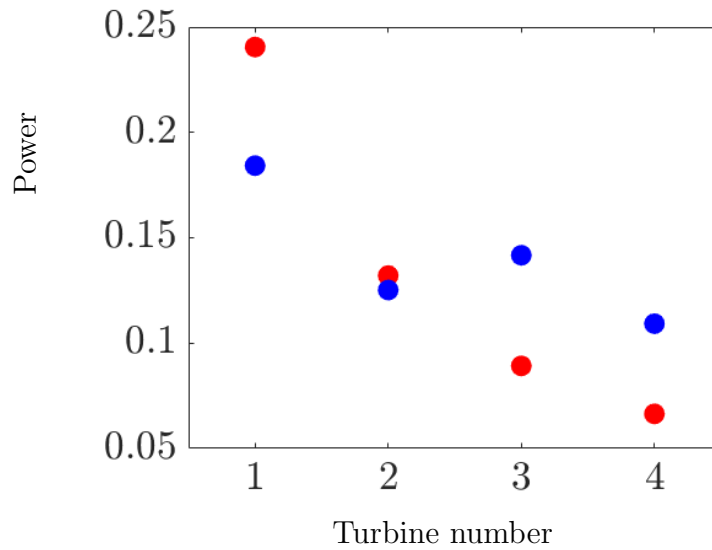


Figure 5.2. Case I: Initial (red) versus maximum (blue) power outputs for each turbine.

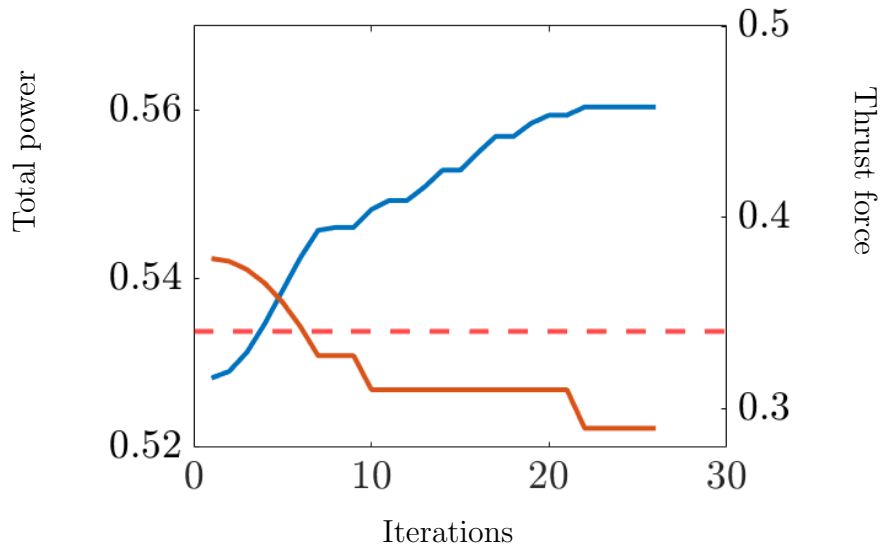


Figure 5.3. Case II: Total power (represented by the blue line and measured along the y axis on the left hand side) and maximum thrust forces (represented by the red line and measured along the y axis on the right hand side) over infinite horizon iterations. The limiting thrust force is represented as the red dashed line.

simulations is displayed in Figure 5.4. We attain a power of 0.606 units and 0.604 units when separately factoring in the uncertainty from the wind turbulence and both, wind turbulence and yaw error, respectively.

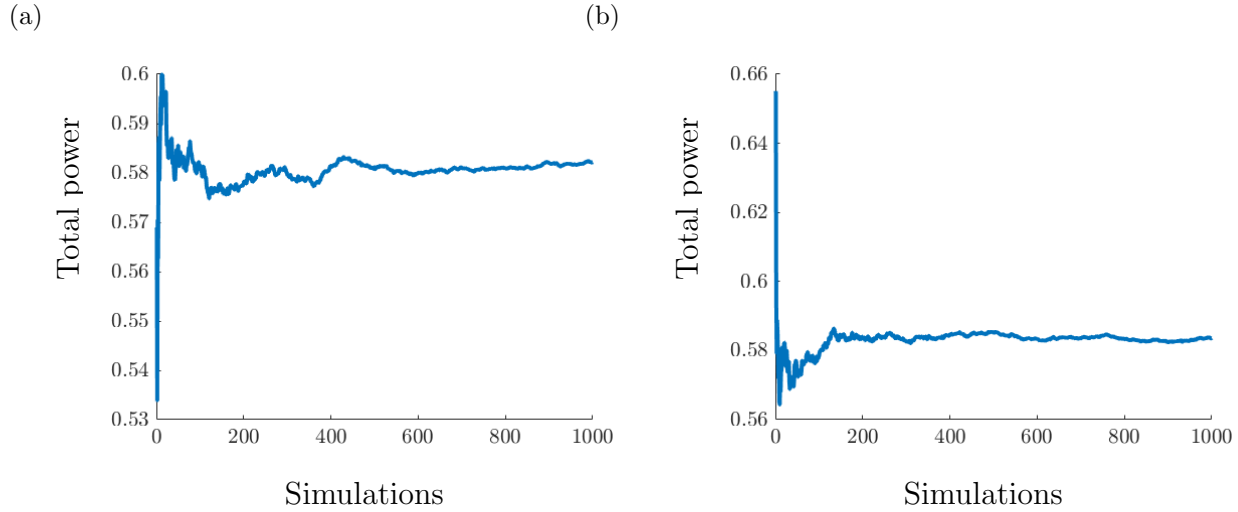


Figure 5.4. Monte Carlo simulations for Case I considering (a) wind variations alone; and (b) wind variations and yaw variations.

Case II: The convergence of the optimal policy can be observed in Figure 5.3 and is achieved when the first 3 turbines are misaligned at 40° and no misalignment exists for the last turbine. As expected, this case study required more iterations to converge upon an optimal policy relative to Case I. Stricter, by which we mean lower, limits on the permissible thrust force also leads to a rise in computations. We note that reasonable limits still have to be imposed as we have little control over the inflow velocity to the first turbine. Also, additional Monte Carlo simulations were required to converge upon power estimations given stochasticity in the states or stochasticity in both states and inputs. For this case study, we converge upon a total power of approximately 0.57 units in both sets of Monte Carlo simulations (Figure 5.5).

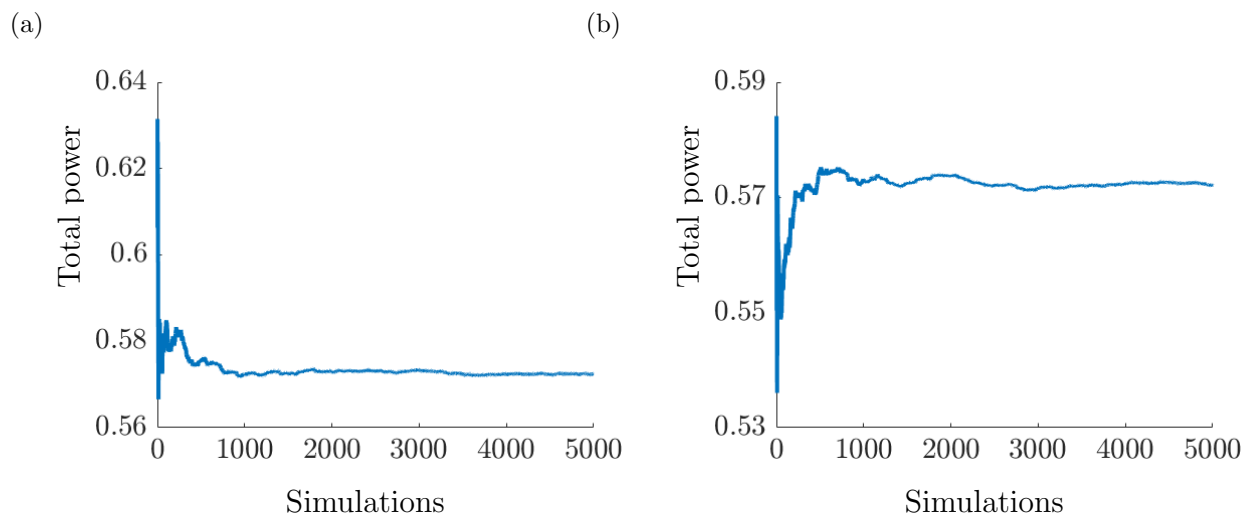


Figure 5.5. Monte Carlo simulations for Case II considering (a) wind variations alone; and (b) wind variations and yaw variations.

CHAPTER 6

CONCLUDING REMARKS

6.1 Conclusions

The inadequacies in predictions of currently available static engineering wake models have necessitated the development of the stochastic dynamical models presented in this thesis. Our models are able to augment the predictions of analytical wake models to describe statistical signatures of wake turbulence in accordance with high-fidelity models. Specifically, we use convex optimization to determine the stochastic excitation that drives the stochastic output of linear dynamic approximations to the governing equations in order to match velocity variances that are prescribed by simulations or experiments at prespecified spatial locations across a wind farm. Our proposition is applicable to operating conditions in wind farms that experience the added complexities due to yaw misalignment.

We support our methodology by providing accurate predictions of directional turbulence in hub-height sectional and 3D models of turbulence. The robustness is emphasized in the quality of results that prevail even when the areas of interest are spread outside of prospective sensor placement. The combination of physical modeling techniques with numerical simulations presents an efficient class of models that use prior training information to save computational effort. It is well-suited to real-time forecasting as the computationally intensive steps in our modeling procedure are conducted offline. Our approach is amenable to the considerations of recently proposed complex variants of analytical wake models that account for the blade geometry and pitch effects that influence the evolution of wakes.

The thrust force exerted on the rotor disc is one of the factors that influences the component loads of a turbine. Higher loads result in an acceleration of structural failures and thereby a reduction in the life span of a wind turbine. In the final chapter of this thesis, we propose a simple control algorithm for optimizing power production across a wind farm

while regulating thrust force levels below prespecified limits that respects the projected life of the turbine. Assuming constant power and thrust force coefficients, we consider both the captured power and exerted thrust force to be linearly dependant on the projected rotor area and functions of an order of the incident velocity. This raises a conflict in optimizing each of them. We demonstrate that a infinite-horizon stopping algorithm is capable of identifying optimal turbine rotor orientations that achieve maximum cumulative power production while respecting prescribed bounds on the thrust force of individual turbines.

6.2 Ongoing efforts

The work conducted in this thesis is inline with our envisioned real-time short-term wind forecasting strategy, which utilizes Kalman filtering algorithms to assimilate real-time ground-level air pressure measurements from across the farm into predictive dynamical models of wind farm turbulence. Ongoing efforts may involve the utility of the 3D models proposed in this thesis for real-time wind forecasting, and the use of alternative covariance completion formulations [24, 67, 69]. The latter is aimed at providing useful information about critical directions and feedback interactions that have maximal effect in bringing model (in our case the stochastically forced linearized NS) and statistics in agreement. Given the physics-based nature of our models, this research direction can prove decisive in identifying salient dynamical couplings and interactions in turbine wakes thereby opening the door to new classes of low-fidelity wake models.

APPENDIX A

SUPERPOSITION TECHNIQUES ON IDENTITY FORCED RESULTS

The multi-turbine system that we model in Section 4.1 needs to account for the cumulative wake flows resulting from the interaction of multiple wakes. This is achieved by calculating stand-alone velocities and then superposing them to model their overlapping effects. The three superposition principles presented in this work (Equations (2.3), (2.4), and (2.5)) may also result in differences in the outcome of variance amplification due to stochastic excitation of the linearized fluctuation dynamics. Here, we study the sensitivity of the modeling framework of Chapter 3 to base flow variation dictated by these superposition techniques.

An exercise with the set of base flows from Figure 2.2 was conducted while exciting our stochastic model with white noise. As shown in Figure 2.2, different superposition principles result in similar waked velocities behind the first two turbines but differences in the wake of downwind turbines. In spite of such differences in the base flow profiles, the variance amplification obtained from solving the Lyapunov equation exhibits almost identical spatial patterns throughout the wind farm (Figure. A.1).

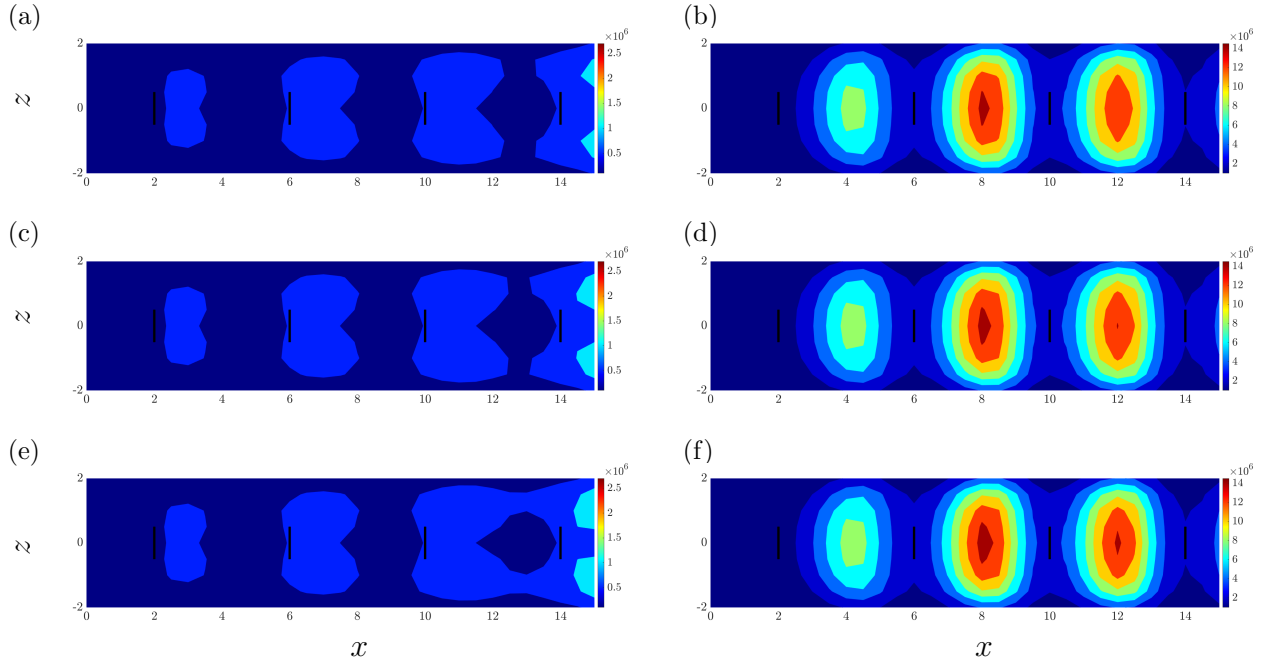


Figure A.1. The streamwise uu (left) and spanwise ww (right) velocity variances as a result of white-in-time forcing of the linearized dynamics of the hub-height velocity fluctuations for a cascade of 4 turbines. The base velocity profiles are obtained using superposition principles from: first row: Equation (2.3); second row: Equation (2.4); and third row: Equation (2.5).

APPENDIX B

RESULTS FROM HIGHER MISALIGNMENTS

While we focus our efforts in Section 4.1.1 to settings typical to maximum power generation, the yaw angles under study have been limited to below 40° of misalignment since angles higher than this are ill-suited to power production cases [27]. We consider here a misalignment of $\gamma = 45^\circ$ and display the quality of covariance completion in Figure B.1 under the same settings as in Section 4.1. We note that the self-similar Gaussian distribution (Section 2.1) is more appropriate to lower angles of yaw [6] and therefore, may not be the best representation of the base velocity $\bar{\mathbf{u}}$ for a rotor yawed at $\gamma = 45^\circ$. We observe regions of irregular predictions in both uu and ww predictions and while further investigation is required into this behaviour, we work on bettering our results for the more likely cases involving lower yaw angles. We do, however, note the better matches between our model and the LES within the regions of the training data.

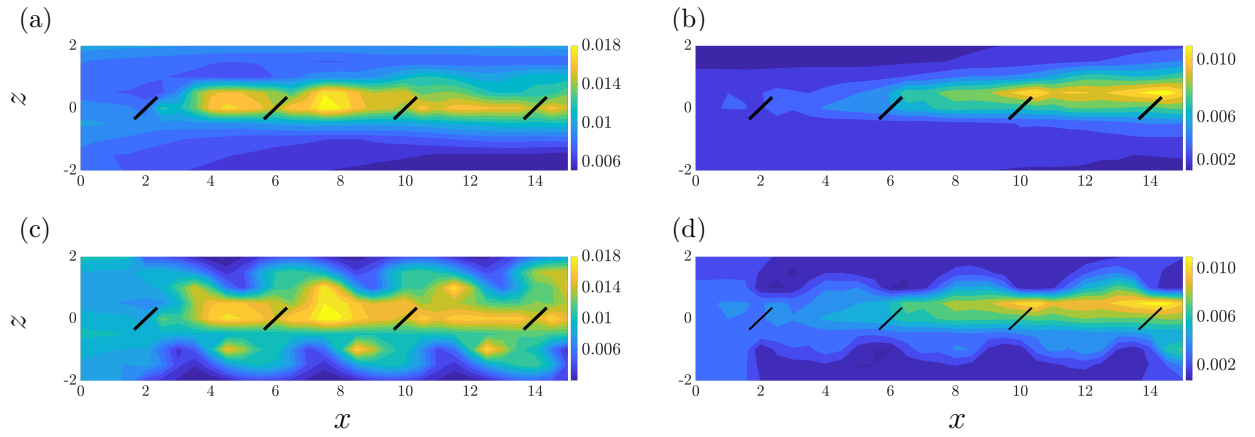


Figure B.1. The streamwise uu (left) and spanwise ww (right) velocity variances at the hub height of a cascade of 4 turbines with uniform yaw angles of 45° (e,f,g,h) resulting from LES (a,b) and our stochastic dynamical model (c,d).

APPENDIX C

COMPARISON STUDY OF CURLED WAKE PARAMETERS

The plane-marching problem formulated to obtain the curled wake profile of the yawed turbine in Section 2.2 was highly sensitive to small parametric variations pertinent to the physical properties of the fluid flow (e.g., Reynolds number) and spatial discretization scheme. In this appendix, we compare the curled velocity profiles that result from changes to such parameters.

C.1 Shear profile at the inflow

Using the power law with a shear exponent of $\alpha = 0.20$ [13] to specify the base velocity component of the curl profile is more accurate, however, it tends to lead to changes in the perturbation velocity in regions outside the wake at greater distances downstream, which is inaccurate and does not contribute to the stability of the numerical solution. However, considering a uniform inflow leads to a more stable solutions. Figure C.1 displays the stream-line base velocity 6 diameters downstream to the turbine with different inflow conditions. We note the visible change in profile at the bottom-right of Figure C.1(b) due to the lower velocity close the the ground.

C.2 Reynolds number

The recommended [42] Reynolds number to formulate the stabilizing viscosity (Equation (2.12)) was 10^4 , however, the value used in these numerical experiments is 10^8 . The numerical stability criterion is easier to achieve with the lower Reynolds number and therefore, our numerical experiments exhibited a few scattered cells of numerical instability, while the recommended value exhibited none. Nevertheless, we continue to use the higher Reynolds number based on the rotor diameter and the free-stream velocity, in accordance with the LES simulations.

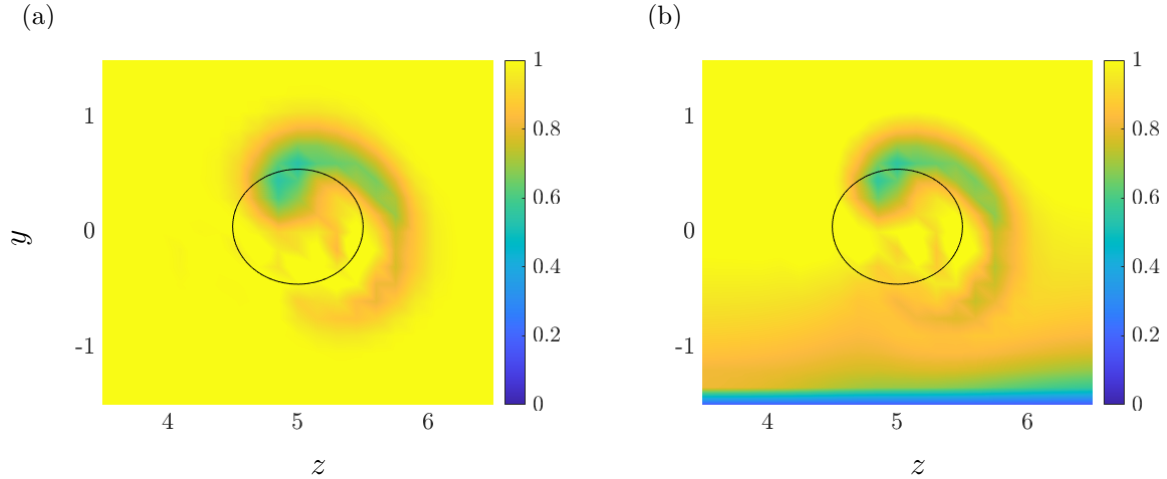


Figure C.1. The streamwise velocity profile at $6 d_0$ downstream of the turbine when considering (a) uniform inflow to the turbine, and (b) atmospheric boundary layer inflow.

C.3 Wake rotation in cross-plane velocity components

The asymmetrical profile of the curled wake that we use in our model (Figure C.2(b)) is due to influence of the wake rotation in the base velocity components. This disproportion between the top and bottom regions of the wake are not present when only the shed tip vortices are considered in Equation (2.8) (See Figures C.2(a) and C.2(c)). We also notice that in the absence of the wake rotation, the bottom of the wake profile interacts more with the velocity gradient closer to the ground; this is prevalent when applying the shear profile to the inflow (Figure C.2(a)) as opposed to a uniform velocity profile in Figure C.2(d).

C.4 Effect of grid size

When the resolution of the finite difference grid required for a suitable calculation of the base velocity is very high, the equations and matrix size required to solve the stochastic dynamic modeling framework described in Chapter 3 become larger and more cumbersome to solve. We therefore, seek to reduce the size of the domain without impacting the integrity of the resulting profile. We found that increasing the grid size in the streamwise dimension caused

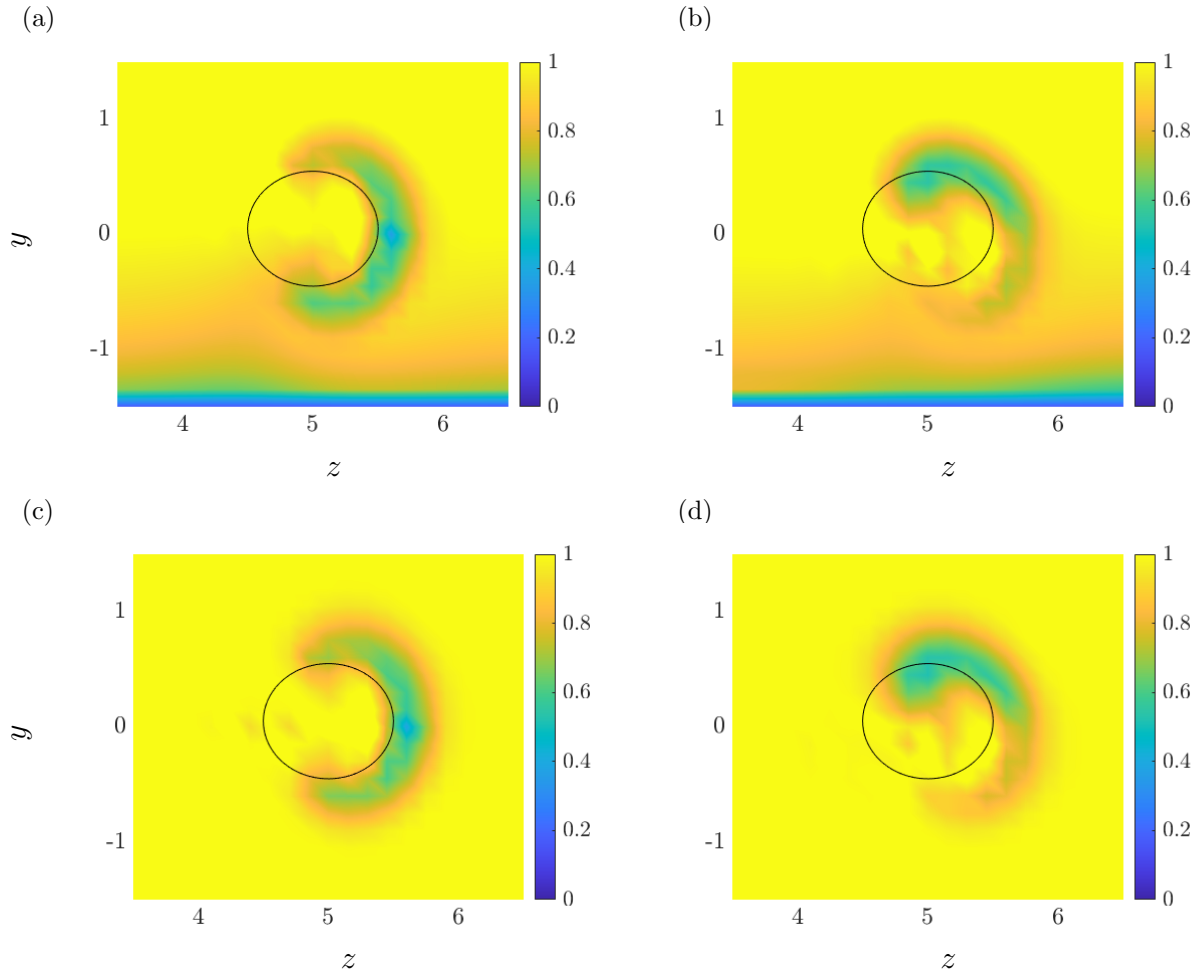


Figure C.2. The streamwise velocity profile at $5 d_0$ downstream of the turbine when considering the atmospheric boundary layer (a, b) and uniform inflow to the turbine (c, d) while using only the shed vortices in the vorticity formulation (a, c) and both shed vortices and the wake rotation vortex in vorticity formulation (b, d).

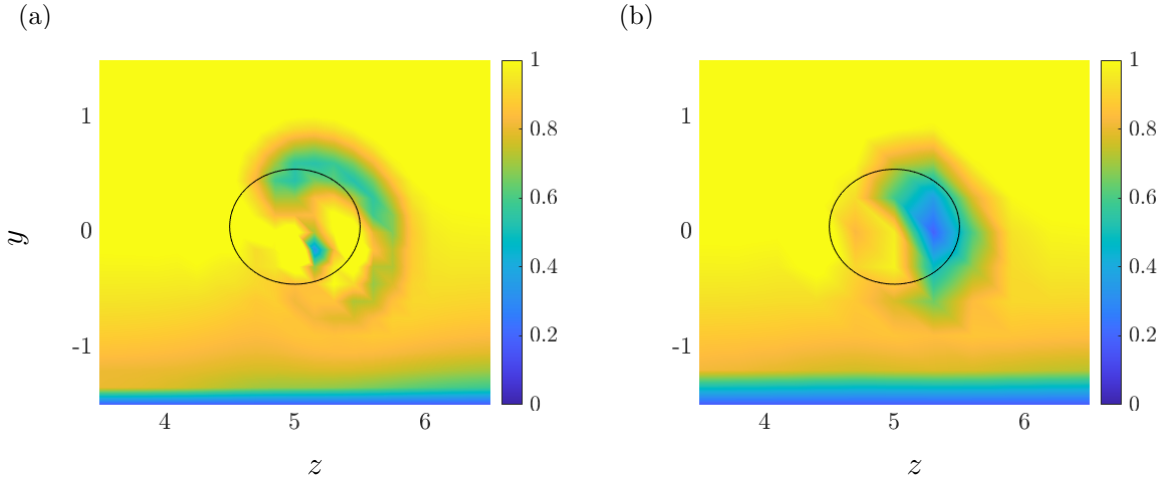


Figure C.3. The streamwise velocity profile at $5 d_0$ downstream of the turbine when considering (a) coarser grid in the streamwise direction, and (b) coarser grid in the spanwise and wall-normal direction.

the most numerical noise in the far-wake region (see Figure C.3(a)), while increases in the spanwise and wall-normal dimensions led to a coarser velocity profile (see Figure C.3(b)), albeit with fewer numerical instabilities. It is important to note, however, that the aspect ratio between the grid sizes in all three dimensions is an important factor in the numerical stability criteria of the model.

BIBLIOGRAPHY

- [1] Abkar, M., J. N. Sørensen, and F. Porté-Agel (2018). An analytical model for the effect of vertical wind veer on wind turbine wakes. *Energies* 11(7), 1838.
- [2] Ainslie, J. F. (1988). Calculating the flowfield in the wake of wind turbines. *J. Wind Eng. Ind. Aerodyn.* 27(1-3), 213–224.
- [3] Alternative Energy tutorials (2010). Alternative energy tutorials wind turbine design. <https://www.alternative-energy-tutorials.com/wind-energy/wind-turbine-design.html>. Accessed: 2023-07-03.
- [4] Astolfi, D., F. Castellani, M. Becchetti, A. Lombardi, and L. Terzi (2020). Wind turbine systematic yaw error: Operation data analysis techniques for detecting it and assessing its performance impact. *Energies* 13(9), 2351.
- [5] Bastankhah, M. and F. Porté-Agel (2014). A new analytical model for wind-turbine wakes. *Renewable energy* 70, 116–123.
- [6] Bastankhah, M. and F. Porté-Agel (2016). Experimental and theoretical study of wind turbine wakes in yawed conditions. *J. Fluid Mech.* 806, 506–541.
- [7] Bastankhah, M., C. R. Shapiro, S. Shamsoddin, D. F. Gayme, and C. Meneveau (2022). A vortex sheet based analytical model of the curled wake behind yawed wind turbines. *J. Fluid Mech.* 933, A2.
- [8] Bay, C. J., P. Fleming, B. Doekemeijer, J. King, M. Churchfield, and R. Mudafort (2022). Addressing deep array effects and impacts to wake steering with the cumulative-curl wake model. *Wind Energy Science Discussions* 2022, 1–28.
- [9] Bellman, R. E. (2010). *Dynamic programming*. Princeton university press.
- [10] Bertsekas, D. (2012). *Dynamic programming and optimal control: Volume I*, Volume 1. Athena scientific.
- [11] Bhatt, A. H., F. Bernardoni, S. Leonardi, and A. Zare (2022). Stochastic dynamical wake modeling for wind farms. *Wind Energy*. Submitted.
- [12] Bhatt, A. H. and A. Zare (2022). Toward stochastic dynamical wake-modeling for wind farms. In *Proceedings of the 2022 American Control Conference*, pp. 5241–5246.
- [13] Burton, T., N. Jenkins, D. Sharpe, and E. Bossanyi (2011). *Wind energy handbook*. John Wiley & Sons.

- [14] Chamorro, L. P. and F. Porté-Agel (2009). A wind-tunnel investigation of wind-turbine wakes: boundary-layer turbulence effects. *Boundary-layer meteorology* 132, 129–149.
- [15] Chamorro, L. P. and F. Porté-Agel (2010). Effects of thermal stability and incoming boundary-layer flow characteristics on wind-turbine wakes: a wind-tunnel study. *Boundary-layer meteorology* 136, 515–533.
- [16] Child, M., C. Kemfert, D. Bogdanov, and C. Breyer (2019). Flexible electricity generation, grid exchange and storage for the transition to a 100% renewable energy system in europe. *Renewable Energy* 139, 80–101.
- [17] EIA (2021a). Renewables account for most new u.s. electricity generating capacity in 2021. <https://www.eia.gov/todayinenergy/detail.php?id=46416>. Accessed: 2023-06-08.
- [18] EIA (2021b). Use of electricity in houses to grow more quickly in developing economies. <https://www.eia.gov/todayinenergy/detail.php?id=50256>. Accessed: 2023-06-08.
- [19] Fang, K., Y. Zhou, S. Wang, R. Ye, and S. Guo (2018). Assessing national renewable energy competitiveness of the g20: A revised porter’s diamond model. *Renewable and Sustainable Energy Reviews* 93, 719–731.
- [20] Fazel, M. (2002). *Matrix rank minimization with applications*. Ph. D. thesis, Stanford University.
- [21] Frandsen, S., R. Barthelmie, S. Pryor, O. Rathmann, S. Larsen, J. Højstrup, and M. Thøgersen (2006). Analytical modelling of wind speed deficit in large offshore wind farms. *Wind Energy: An International Journal for Progress and Applications in Wind Power Conversion Technology* 9(1-2), 39–53.
- [22] Gaumont, M., P.-E. Réthoré, S. Ott, A. Pena, A. Bechmann, and K. S. Hansen (2014). Evaluation of the wind direction uncertainty and its impact on wake modeling at the horns rev offshore wind farm. *Wind Energy* 17(8), 1169–1178.
- [23] Gould, B. and D. Burris (2016). Effects of wind shear on wind turbine rotor loads and planetary bearing reliability. *Wind Energy* 19(6), 1011–1021.
- [24] Grussler, C., A. Zare, M. R. Jovanovic, and A. Rantzer (2016). The use of the r^* heuristic in covariance completion problems. In *Proceedings of the 55th IEEE Conference on Decision and Control*, Las Vegas, NV, pp. 1978–1983.
- [25] Haapala, K. R. and P. Prempreeda (2014). Comparative life cycle assessment of 2.0 mw wind turbines. *International Journal of Sustainable Manufacturing* 3(2), 170–185.

- [26] Howland, M. F., J. Bossuyt, L. A. Martínez-Tossas, J. Meyers, and C. Meneveau (2016). Wake structure in actuator disk models of wind turbines in yaw under uniform inflow conditions. *Journal of Renewable and Sustainable Energy* 8(4), 043301.
- [27] Husaru, D. E., P. D. Bârsănescu, and D. Zahariea (2019). Effect of yaw angle on the global performances of horizontal axis wind turbine - QBlade simulation. *IOP Conference Series: Materials Science and Engineering* 595(1), 012047.
- [28] IRENA (2022). Renewable power generation costs in 2021. Technical report, International Renewable Energy Agency, Abu Dhabi.
- [29] Jansen, M., I. Staffell, L. Kitzing, S. Quoilin, E. Wiggelinkhuizen, B. Bulder, I. Riepin, and F. Müsgens (2020). Offshore wind competitiveness in mature markets without subsidy. *Nature Energy* 5(8), 614–622.
- [30] Jensen, N. O. (1983). *A note on wind generator interaction*, Volume 2411. Citeseer.
- [31] Jonkman, J., S. Butterfield, W. Musia, and G. Scott (2009). Definition of a 5-MW reference wind turbine for offshore system development. Technical report, National Renewable Energy Lab. (NREL), Golden, CO, USA.
- [32] Jovanovic, M. R. and B. Bamieh (2005, July). Componentwise energy amplification in channel flows. *J. Fluid Mech.* 534, 145–183.
- [33] Katic, I., J. Højstrup, and N. O. Jensen (1986). A simple model for cluster efficiency. In *European wind energy association conference and exhibition*, Volume 1, pp. 407–410.
- [34] Khadra, K., P. Angot, S. Parneix, and J. Caltagirone (2000). Fictitious domain approach for numerical modelling of Navier-Stokes equations. *Int. J. Numer. Methods Fluids* 34(8), 651–684.
- [35] King, J., P. Fleming, R. King, L. A. Martínez-Tossas, C. J. Bay, R. Mudafort, and E. Simley (2021). Control-oriented model for secondary effects of wake steering. *Wind Energy Science* 6(3), 701–714.
- [36] Krogstad, P.-Å. and P. A. Davidson (2012). Near-field investigation of turbulence produced by multi-scale grids. *Physics of Fluids* 24(3), 035103.
- [37] Li, L., Z. Huang, M. Ge, and Q. Zhang (2022). A novel three-dimensional analytical model of the added streamwise turbulence intensity for wind-turbine wakes. *Energy* 238, 121806.
- [38] Lin, Z. and X. Liu (2020). Wind power forecasting of an offshore wind turbine based on high-frequency scada data and deep learning neural network. *Energy* 201, 117693.

- [39] Lissaman, P. (1979). Energy effectiveness of arbitrary arrays of wind turbines. *Journal of Energy* 3(6), 323–328.
- [40] Mani, A. (2012). Analysis and optimization of numerical sponge layers as a nonreflective boundary treatment. *J. Comput. Phys.* 231(2), 704–716.
- [41] Markfort, C. D., W. Zhang, and F. Porté-Agel (2012). Turbulent flow and scalar transport through and over aligned and staggered wind farms. *Journal of Turbulence* 13(1), N33.
- [42] Martínez-Tossas, L. A., J. Annoni, P. A. Fleming, and M. J. Churchfield (2019). The aerodynamics of the curled wake: a simplified model in view of flow control. *Wind Energy Science* 4(1), 127–138.
- [43] Martínez-Tossas, L. A. and E. Branlard (2020). The curled wake model: equivalence of shed vorticity models. In *J. Phys. Conf. Ser.*, Volume 1452, pp. 012069. IOP Publishing.
- [44] Medici, D. and P. H. Alfredsson (2006). Measurements on a wind turbine wake: 3D effects and bluff body vortex shedding. *Wind Energy* 9(3), 219–236.
- [45] Menezes, E. J. N., A. M. Araújo, J. S. Rohatgi, and P. M. G. del Foyo (2018). Active load control of large wind turbines using state-space methods and disturbance accommodating control. *Energy* 150, 310–319.
- [46] Milligan, M., M. N. Schwartz, and Y.-h. Wan (2003). Statistical wind power forecasting for US wind farms. Technical report, National Renewable Energy Lab., Golden, CO (US).
- [47] Mohammadi, M., M. Bastankhah, P. Fleming, M. Churchfield, E. Bossanyi, L. Landberg, and R. Ruisi (2022). Curled-skewed wakes behind yawed wind turbines subject to veered inflow. *Energies* 15(23), 9135.
- [48] Niayifar, A. and F. Porté-Agel (2016). Analytical modeling of wind farms: A new approach for power prediction. *Energies* 9(9), 741.
- [49] Nichols, J. W. and S. K. Lele (2011). Global modes and transient response of a cold supersonic jet. *J. Fluid Mech.* 669, 225–241.
- [50] Pope, S. B. (2000). *Turbulent flows*. Cambridge University Press.
- [51] Ran, W., A. Zare, M. J. P. Hack, and M. R. Jovanovic (2019, September). Stochastic receptivity analysis of boundary layer flow. *Phys. Rev. Fluids* 4(9), 093901 (28 pages).
- [52] Ran, W., A. Zare, and M. R. Jovanović (2021, January). Model-based design of riblets for turbulent drag reduction. *J. Fluid Mech.* 906, A7 (38 pages).

- [53] Ran, W., A. Zare, J. W. Nichols, and M. R. Jovanovic (2017). The effect of sponge layers on global stability analysis of blasius boundary layer flow. In *Proceedings of the 47th AIAA Fluid Dynamics Conference*, Denver, CO, pp. 3456 (12 pages).
- [54] Recht, B., M. Fazel, and P. A. Parrilo (2010). Guaranteed minimum-rank solutions of linear matrix equations via nuclear norm minimization. *SIAM Rev.* 52(3), 471–501.
- [55] Santoni, C., K. Carrasquillo, I. Arenas-Navarro, and S. Leonardi (2017). Effect of tower and nacelle on the flow past a wind turbine. *Wind Energy* 20(12), 1927–1939.
- [56] Santoni, C., E. J. García-Cartagena, U. Ciri, L. Zhan, G. V. Iungo, and S. Leonardi (2020). One-way mesoscale-microscale coupling for simulating a wind farm in North Texas: Assessment against SCADA and LiDAR data. *Wind Energy* 23(3), 691–710.
- [57] Susan Dlin (2022). S&p global market intelligence. <https://www.spglobal.com/marketintelligence/en/news-insights/latest-news-headlines/nearly-28-gw-of-new-us-generating-capacity-added-in-2021-led-by-wind-68435915>. Accessed: 2023-07-03.
- [58] UNDP, UNOHRLLS, World Bank, and TWG Members (2021). Theme report on energy access. Technical report, United Nations.
- [59] Veers, P., K. Dykes, E. Lantz, S. Barth, C. L. Bottasso, O. Carlson, A. Clifton, J. Green, P. Green, H. Holttinen, et al. (2019). Grand challenges in the science of wind energy. *Science* 366(6464), eaau2027.
- [60] Voutsinas, S., K. Rados, and A. Zervos (1990). On the analysis of wake effects in wind parks. *Wind Engineering* 14(4), 204–219.
- [61] Wan, S., L. Cheng, and X. Sheng (2015). Effects of yaw error on wind turbine running characteristics based on the equivalent wind speed model. *Energies* 8(7), 6286–6301.
- [62] Wind Energy Technologies Office (2023). Wind energy basics. <https://www.energy.gov/eere/wind/wind-energy-basics>. Accessed: 2023-07-03.
- [63] Wu, Y.-K. and J.-S. Hong (2007). A literature review of wind forecasting technology in the world. In *2007 IEEE Lausanne Power Tech*, pp. 504–509.
- [64] Zare, A., Y. Chen, M. R. Jovanovic, and T. T. Georgiou (2017, March). Low-complexity modeling of partially available second-order statistics: theory and an efficient matrix completion algorithm. *IEEE Trans. Automat. Control* 62(3), 1368–1383.
- [65] Zare, A., T. T. Georgiou, and M. R. Jovanovic (2020, May). Stochastic dynamical modeling of turbulent flows. *Annu. Rev. Control Robot. Auton. Syst.* 3, 195–219.

- [66] Zare, A., M. R. Jovanovic, and T. T. Georgiou (2014). Completion of partially known turbulent flow statistics. In *Proceedings of the 2014 American Control Conference*, pp. 1680–1685.
- [67] Zare, A., M. R. Jovanovic, and T. T. Georgiou (2016). Perturbation of system dynamics and the covariance completion problem. In *Proceedings of the 55th IEEE Conference on Decision and Control*, pp. 7036–7041.
- [68] Zare, A., M. R. Jovanovic, and T. T. Georgiou (2017, February). Colour of turbulence. *J. Fluid Mech.* 812, 636–680.
- [69] Zare, A., H. Mohammadi, N. K. Dhingra, T. T. Georgiou, and M. R. Jovanović (2020, August). Proximal algorithms for large-scale statistical modeling and sensor/actuator selection. *IEEE Trans. Automat. Control* 65(8), 3441–3456.
- [70] Zhan, L., S. Letizia, and G. Iungo (2020). Optimal tuning of engineering wake models through lidar measurements. *Wind Energy Science* 5(4), 1601–1622.
- [71] Zhang, W., C. D. Markfort, and F. Porté-Agel (2012). Near-wake flow structure downwind of a wind turbine in a turbulent boundary layer. *Experiments in fluids* 52, 1219–1235.
- [72] Zong, H. and F. Porté-Agel (2020). A point vortex transportation model for yawed wind turbine wakes. *Journal of Fluid Mechanics* 890, A8.

BIOGRAPHICAL SKETCH

Mireille Rodrigues joined The University of Texas at Dallas in the Fall semester of 2021. Previously, she acquired an undergraduate degree in Mechanical Engineering in 2009 and a postgraduate degree in Design Engineering in 2011. Following this, she worked in the wind energy sector for several years.

While at UTD, she conducted research in the field of wind power; specifically into turbulent wake flows in wind farms under the supervision of Dr. Armin Zare. This thesis was created in partial fulfillment of her masters degree in Mechanical Engineering with a concentration area in Dynamics and Systems Control.

CURRICULUM VITAE

Mireille Rodrigues

July 7, 2023

Educational History:

MS, Mechanical Engineering, The University of Texas at Dallas, Dallas, TX, 2023
ME, Design Engineering, Birla Institute of Technology and Science - Pilani, Pilani, IN 2011
BE, Mechanical Engineering, Sathyabama University, Chennai, IN 2009

Employment History:

Student Assistant, The University of Texas at Dallas, Fall '22 - Spr '23
Associate Manager, Siemens Gamesa Renewable Energy, May 2016 – July 2021
Structural Engineer, Vestas Wind Systems, August 2011 – March 2016

Publications and Abstracts:

Robustness of two-dimensional stochastic dynamical wake models for yawed wind turbines

M. Rodrigues, N. A. Burgess, A. H. Bhatt, S. Leonardi, and A. Zare
in Proceedings of the 2023 American Control Conference, 2023, pp. 818–823

Data-enhanced stochastic dynamical modeling of yawed wind turbine wakes

M. Rodrigues, M.V. Lingad, S. Leonardi and A. Zare
in Bulletin of Wind Energy Science Conference, Glasgow, UK, 2023

Stochastic dynamical modeling of wind farm turbulence

A. Zare, A. H. Bhatt, F. Bernardoni, M. Rodrigues and S. Leonardi
in Bulletin of the American Physical Society, Indianapolis, IN, 2022

Academic Projects:

Stochastic dynamical modeling of yawed wind turbine wakes

Worked with Dr. Armin Zare to develop reduced order 2D- and 3D- models of turbulence behind turbine rotors. Used stochastically forced models, incorporating the physical attributes of yawed turbine wakes including deflection, rotation, and curl, to provide the turbulent velocity in wind farms.

Optimal variable yaw control for an ADM wind farm model

Obtained yaw angles corresponding to max power under constrained thrust force using infinite horizon stopping and Monte Carlo simulations in a physics-based actuator disc model four-turbine farm.

Multi-disciplinary optimization of a wind turbine main shaft

Utilized optimization under uncertainty to find optimal distance between bearings while minimizing cost.